REPUBLIC OF TÜRKİYE
YILDIZ TECHNICAL UNIVERSITY
GRADUATE SCHOOL OF SCIENCE AND ENGINEERING

NUMERICAL INVESTIGATION OF THE EFFECT OF FREE SURFACE AND DEPTH ON FLOW-INDUCED NOISE IN A SUBMARINE FORM

Kağan Esat ÖZLÜ

MASTER OF SCIENCE THESIS

Department of Naval Architecture and Marine Engineering

Program of Naval Architecture and Marine Engineering

Supervisor

Asst. Prof. Dr. Ahmet Gültekin AVCI

January, 2025

REPUBLIC OF TÜRKİYE

YILDIZ TECHNICAL UNIVERSITY

GRADUATE SCHOOL OF SCIENCE AND ENGINEERING

NUMERICAL INVESTIGATION OF THE EFFECT OF FREE SURFACE AND DEPTH ON FLOW-INDUCED NOISE IN A SUBMARINE FORM

A thesis submitted by Kağan Esat ÖZLÜ in partial fulfillment of the requirements for the degree of **MASTER OF SCIENCE** is approved by the committee on 21.01.2025 in Department of Naval Architecture and Marine Engineering, Program of Naval Architecture and Marine Engineering.

Asst. Prof. Dr. Ahmet Gültekin AVCI
Yildiz Technical University
Supervisor

Approved By the Examining Committee

Asst. Prof. Dr. Ahmet Gültekin AVCI, Supervisor
Yildiz Technical University _____

Prof. Dr. Seyfettin BAYRAKTAR, Member
Yildiz Technical University _____

Assoc. Prof. Dr. Ali DOĞRUL, Member
National Defence University _____

I hereby declare that I have obtained the required legal permissions during data collection and exploitation procedures, that I have made the in-text citations and cited the references properly, that I haven't falsified and/or fabricated research data and results of the study and that I have abided by the principles of the scientific research and ethics during my Thesis Study under the title of " Numerical Investigation Of The Effect Of Free Surface And Depth On Flow-Induced Noise In A Submarine Form " supervised by my supervisor, Asst. Prof. Dr. Ahmet Gültekin AVCI. In the case of a discovery of false statement, I am to acknowledge any legal consequence.

Kağan Esat ÖZLÜ

Signature

Dedicated to my family

ACKNOWLEDGEMENTS

I would like to express my heartfelt gratitude to my esteemed advisor, Asst. Prof. Dr. Ahmet Gültekin Avcı, for his guidance, expertise, and support throughout this thesis. His encouragement and invaluable insights made this journey both meaningful and productive.

I am also deeply thankful to Assoc. Prof. Dr. Ahmet Yurtseven for his significant contributions to the development of my thesis. His constructive feedback and thoughtful suggestions greatly enhanced the quality of this work and broadened my academic perspective.

During my Erasmus program in Naples, I had the privilege of receiving valuable guidance and support from Prof. Dr. Simone Mancini. I sincerely thank him for his expertise and contributions, which played a pivotal role in improving the depth and scope of this thesis.

I extend my deepest thanks to my family, whose unwavering patience, love, and encouragement have been my greatest source of strength throughout this process. Your constant support has enabled me to overcome every challenge and achieve my goals. This accomplishment would not have been possible without your unconditional love and belief in me.

Lastly, I would like to thank the Türk Loydu Foundation for their support during my master's education.

Kağan Esat Özlü

TABLE OF CONTENTS

LIST OF SYMBOLS

ρ	Density
ρ'	Density Fluctuations
q2	Dipole Sound Sources
F_r	Froude Number
P	Hydrostatic Pressure
δ	Kronecker Delta
T_{ij}	Lighthill Turbulence Stress Tensor
q1	Monopole Sound Sources
q3	Quadrupole Sound Sources
P_{ref}	Reference Pressure
I_{ref}	Reference Sound Intensity Level
W_{ref}	Reference Sound Power
c_0	Reference Sound Speed
I	Sound Intensity Level
W	Sound Power
c	Sound Speed
T	Temperature
t	Time
σ_{ij}	Viscous Stress Tensor

LIST OF ABBREVIATIONS

CAA	Computational Aeroacoustics
CFD	Computational Fluid Dynamics
DARPA	The Defense Advanced Research Projects Agency
dB	Decibel
DES	Detached-Eddy Simulation
DNS	Direct Numerical Simulation
FFT	Fast Fourier Transform
Fr	Froude Number
Fr_h	Depth Froude Number
FVM	Finite Volume Method
FW-H	Ffowcs Williams-Hawking
INSEAN	Italian National Institute For Naval Architecture Studies And Testing
ITTC	International Towing Tank Conference
LES	Large Eddy Simulation
RANS	Reynolds Averaged Navier-Stokes
Re	Reynolds Number
SPL	Sound Pressure Level
TVC	Tip Vortex Cavitation
URANS	Unstady Reynolds Averaged Navier-Stokes
URN	Underwater Radiated Noise
V-AMR	Vortex-Based Actuator Mesh Refinement

LIST OF FIGURES

LIST OF TABLES

ABSTRACT

NUMERICAL INVESTIGATION OF THE EFFECT OF FREE SURFACE AND DEPTH ON FLOW-INDUCED NOISE IN A SUBMARINE FORM

Kağan Esat ÖZLÜ

Department of Naval Architecture and Marine Engineering
Master Program of Naval Architecture and Marine Engineering
Master of Science Thesis

Supervisor: Asst. Prof. Dr. Ahmet Gültekin AVCI

Hydrodynamic noise is critical for submarines to maintain stealth and reduce the risk of detection by enemy sonar systems, ensuring operational security. It also has adverse effects on marine ecosystems, threatening the behavior and habitats of underwater species. Therefore, accurate prediction and mitigation of noise are essential for both military strategies and ecological balance.

Literature studies indicate that noise generated by submarines is classified into three main sources: machinery noise, propeller noise, and hydrodynamic (flow) noise. While hydrodynamic noise is generally at a lower level compared to other sources, its impact increases significantly as submarine speed increases. This makes the examination of flow-induced noise's contribution to the overall acoustic signature crucial.

In this study, the variations of hydrodynamic noise with parameters such as depth and speed were investigated using the DARPA AFF-8 submarine model. The URANS equations were discretized and solved using the finite volume method within the commercial CFD software Siemens STAR-CCM+. Initially, the flow

around the submarine was solved using CFD methods, and the results were validated by comparison with experimental data. Subsequently, the acoustic characteristics of the submarine were analyzed in detail using the Ffowcs Williams-Hawkings (FW-H) method. The analyses showed that as depth increases, vortex volumes decrease, leading to a reduction in acoustic noise levels. Conversely, an increase in speed intensifies turbulence, resulting in higher acoustic noise levels. When the submarine is near the free surface, the dominant frequency amplitude increases with higher velocities due to intensified flow disturbances. As it moves deeper at the same velocity, the dominant frequency decreases as surface effects diminish and the flow stabilizes. This underscores the impact of depth and velocity on acoustic characteristics.

In conclusion, this study highlights the effects of flow parameters such as depth and speed on hydrodynamic noise. These findings may provide critical data for developing strategies to reduce submarine noise levels effectively**.**

Keywords: Flow-induced noise, Ffowcs Williams-Hawkings method.

ÖZET

SERBEST YÜZEY VE DERİNLİK ETKİSİNİN BİR DENİZALTI FORMUNDAKİ AKIŞ KAYNAKLI GÜRÜLTÜYE ETKİSİNİN SAYISAL İNCELENMESİ

Kağan Esat ÖZLÜ

Gemi İnşaatı ve Gemi Makineleri Mühendisliği Anabilim Dalı
Gemi İnşaatı ve Gemi Makineleri Mühendisliği Yüksek Lisans Programı
Yüksek Lisans Tezi

Danışman: Dr. Öğr. Üyesi Ahmet Gültekin AVCI

Hidrodinamik gürültü, denizaltıların gizliliğini koruyarak düşman sonarlarına karşı tespit edilme riskini azaltmak ve operasyonel güvenlik sağlamak için kritik öneme sahiptir. Ayrıca, deniz ekosistemleri üzerinde olumsuz etkiler yaratarak su altı canlılarının davranışlarını ve yaşam alanlarını tehdit edebilir. Bu nedenle, gürültünün doğru tahmini ve azaltılması, hem askeri stratejiler hem de ekolojik denge için hayati bir gerekliliktir.

Literatür çalışmaları, denizaltılar tarafından üretilen gürültünün üç ana kaynağa ayrıldığını göstermektedir: makine gürültüsü, pervane gürültüsü ve hidrodinamik (akış) gürültüsü. Hidrodinamik gürültü, genellikle diğer gürültü kaynaklarına kıyasla daha düşük seviyede olsa da denizaltı hızı arttıkça etkisi önemli ölçüde artmaktadır. Bu durum, akış kaynaklı gürültünün genel akustik imzaya olan katkısının incelenmesini kritik hale getirmektedir.

Bu çalışmada, DARPA AFF-8 denizaltı modeli üzerinde yapılan hesaplamalarla hidrodinamik gürültünün derinlik ve hız gibi parametrelerle nasıl değiştiği incelenmiştir. Ticari bir HAD yazılımı olan Siemens STAR-CCM+ kullanılarak URANS denklemleri sonlu hacimler yöntemiyle ayrıklaştırılmış ve çözülmüştür. İlk aşamada, denizaltı etrafındaki akış HAD yöntemleriyle çözülmüş, elde edilen

sonuçlar deneysel verilerle karşılaştırılarak doğrulanmıştır. Daha sonra, Ffowcs Williams-Hawkings (FW-H) yöntemi kullanılarak denizaltının akustik özellikleri detaylı bir şekilde analiz edilmiştir. Analizler, derinliğin artmasıyla birlikte girdap hacimlerinin küçüldüğünü ve buna bağlı olarak akustik gürültü seviyesinin azaldığını göstermiştir. Hızın artması durumunda ise türbülans şiddetinin yükseldiği ve bunun akustik gürültü seviyelerini artırdığı tespit edilmiştir. Denizaltı serbest su yüzeyine yakın olduğunda, artan hızla birlikte baskın frekans genliği yüzeyle etkileşimlerden dolayı artar. Aynı hızda daha derine inildikçe, yüzey etkileri azaldığı ve akış stabilize olduğu için baskın frekans azalır. Bu durum, derinlik ve hızın akustik özellikler üzerindeki etkisini vurgulamaktadır.

Sonuç olarak, bu çalışma, derinlik ve hız gibi akış parametrelerinin hidrodinamik gürültü üzerindeki etkilerini ortaya koymuş ve bu bulgular, denizaltıların gürültü seviyelerinin azaltılmasına yönelik stratejilerin geliştirilmesi için önemli veriler sağlayabilecektir.

Anahtar Kelimeler: Akış kaynaklı gürültü, Ffowcs Williams-Hawkings yöntemi.

1
INTRODUCTION

1.1 What Is The Significance Of Hydrodynamic Noise

The prediction of hydrodynamic noise holds great significance for several key reasons. Firstly, submarines play a crucial role in naval operations, and their capacity for discreet operation is paramount. The prediction and reduction of hydrodynamic noise are instrumental in rendering submarines less detectable by underwater sonar systems, a vital factor in ensuring their security and efficacy in military endeavors. Minimizing hydrodynamic noise enhances the operational efficiency of submarines, enabling them to approach targets or engage in surveillance without arousing the attention of potential adversaries, thereby enhancing their strategic advantage. Submarines hold a central position in the national security strategies of numerous nations. Precise forecasting and management of hydrodynamic noise play a pivotal role in global security by bolstering the operational efficiency of submarine fleets and diminishing the likelihood of detection by potential foes.

The ability of a warship or submarine to detect other vessels before being detected by them holds significant strategic importance and often determines the fate of the ship and its personnel in numerous scenarios. This can only be achieved through the ship being quieter than enemy vessels and possessing superior sonar systems compared to them.

Secondly, Submarines operations can influence marine ecosystems, particularly in their operational zones. The ability to predict and control hydrodynamic noise is crucial for mitigating disruptions to aquatic life. This conservation effort plays a pivotal role in preserving marine habitats and safeguarding endangered species. Excessive noise can disrupt their natural behavior, affect their feeding patterns, and

even lead to habitat displacement or injury. Therefore, by accurately predicting and minimizing noise, we can help mitigate potential adverse effects on marine ecosystems and preserve their delicate balance.

In summary, predicting hydrodynamic noise plays a critical role in enhancing the stealth capabilities of military ships, increasing their detectability by enemy vessels. Additionally, it is important for safeguarding marine ecosystems by minimizing noise-related disturbances to underwater animals. By understanding and addressing the factors influencing hydrodynamic noise, we can work towards creating quieter and more environmentally friendly maritime systems while maintaining a tactical advantage in naval operations.

1.2 Aim Of Thesis

The aim of this study is to accurately predict the flow-induced noise generated around submarines using Computational Fluid Dynamics (CFD) techniques. By employing Ffowcs Williams-Hawkings (FW-H) equations for far-field noise estimation, the study seeks to provide a reliable framework for evaluating acoustic performance. Through precise resolution of the flow around the submarine and subsequent noise analysis, this work aspires to contribute to the literature by offering insights into the acoustic behavior and enhancing the understanding of submarine noise generation mechanisms.

1.3 Lirerature Review

The noise generated by submarines can be categorized according to Ross [1] into three distinct types:

- Machinery noise is a result of the operation of both the main propulsion system and auxiliary equipment.
- Propeller noise arises from flow phenomena occurring on the propeller as it operates within the wake field of the ship's hull.
- Hydrodynamic (flow) noise originates from the flow of water along the surface of the ship's hull.

In general, hydrodynamic noise typically has a lower sound pressure level compared to mechanical propeller noise and vibration noise. Nevertheless, with the

acceleration of the submarine's speed, the impact of hydrodynamic noise on the overall sound pressure level of the submarine will increase significantly.

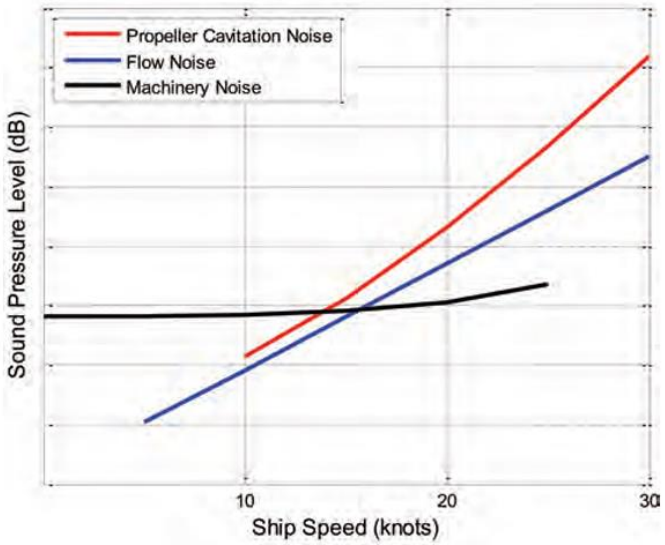

Figure 1.1 Representation depicting how the contributors to underwater radiated noise (URN) from a ship change as ship speed varies [2].

Machinery noise is considered structure-borne noise because it arises from the ship's structure being stimulated by the machinery equipment.

On the other hand, the remaining two categories produce fluid-borne noise. The mechanisms responsible for generating noise in each category may vary in nature. Instances of noise stemming from mechanical sources encompass situations such as rotating unbalance, combustion processes, and friction in bearings.

Fluid flow phenomena, such as turbulence, cavitation, vortex shedding, displacement, and lift are responsible for generating both linear field pressure fluctuations and radiated noise. Propeller noise consists of two components: non-cavitating propeller noise and cavitation noise. When cavitation occurs, it usually becomes the predominant source of noise, as shown in Figure 1.1. Typically, cavitation initially occurs on the propeller and only at high ship speeds extends to affect struts, rudders, and stabilizers. Consequently, the majority of efforts related to hydrodynamic ship noise mitigation are directed towards addressing propeller cavitation noise.

The first studies on flow-induced noise date back to 1878 when Strouhal investigated wind-induced noise generated around a cylinder. In this pioneering

work, Strouhal analyzed the periodic forces caused by the flow around the cylinder and the subsequent sound waves produced. His findings were instrumental in understanding flow-structure interaction phenomena and laid the foundation for modern fields such as aeroacoustics and hydroacoustics. Strouhal's research introduced the concept of the Strouhal Number, which describes the relationship between the frequency of vortex shedding, the characteristic dimensions of an object, and the flow velocity. This dimensionless parameter has since become a critical tool in analyzing flow-induced vibrations and noise in engineering applications.

Lighthill introduced the acoustic analogy theory in the 1950s to study aerodynamic noise, which later became a foundational framework for understanding flow-induced noise in various applications, including underwater vehicles. This theory marked a significant advancement by integrating sound field calculations with flow field calculations for the initial time. It enabled the acquisition of flow field information by solving the acoustic field, resulting in a substantial enhancement in the computational efficiency for predicting URN [3], [4]. It's important to acknowledge that this approach overlooks the dynamic reactions of the shell structure in response to unsteady fluid pressures.

In addition to Lighthill's groundbreaking research, Proudman also contributed significantly to the field by investigating noise generation due to isotropic turbulence in the same year. Proudman's work complemented Lighthill's theoretical framework by focusing on turbulence-induced noise, an essential aspect of flow acoustics. Building upon these foundational studies, Curle further advanced the field in 1955 by addressing the interaction between solid surfaces and surrounding fluid flows, thereby extending Lighthill's acoustic analogy to account for the effects of rigid body boundaries.

The most notable development came in 1969, when Ffowcs Williams and Hawkings proposed a generalization of Lighthill's equation to encompass noise generation from arbitrary-shaped bodies in motion. Their formulation introduced an innovative approach to calculate acoustic emissions resulting from the interaction of unsteady flows with moving or stationary surfaces. This work became a cornerstone in computational aeroacoustics (CAA) and hydroacoustics, enabling the precise prediction of noise from complex geometries such as aircraft, submarine

hulls, and propellers. Ffowcs-Williams and Hawkings have identified three distinct noise sources in the FW–H equation, namely monopole, dipole, and quadrupole noise. There are various methods available for assessing these noise sources [5].

Farassat [6], Farassat and Succi [7], and Farassat [8], [9] subsequently developed multiple integral representations of the FW-H equation which are suitable for various motions in both subsonic and supersonic flows. These integral representations provide solutions to acoustic problems, presuming that the geometric properties of a moving entity, its temporal path, and surface loadings are pre-established via separate hydrodynamic analyses.

Wang and colleagues utilized Large Eddy Simulation (LES) and Lighthill acoustic simulation techniques to forecast the flow noise originating from an underwater vehicle. They investigated the variations in noise features along both transverse and axial directions, as well as the radiation directivity and sound energy. Furthermore, they conducted an analysis of the flow noise produced by the sail and propeller [10].

To assess the impact of rudders at stern to the hydrodynamic noise features of underwater vehicles, Shi Yao and colleagues performed a numerical simulation of the flow field and hydrodynamic noise on DARPA SUBOFF using the Lighthill acoustic simulation and LES technique. Their analysis revealed that the noise generated by X-type rudders was 3 dB lower than produced by cross-type rudders [11].

Yu and colleagues conducted measurements of the far-field noise generated by an Autonomous Underwater Vehicle (AUV) under various operational scenarios. They also forecasted the flow radiated noise of the AUV by utilizing a combination of CFD and the Lighthill equation. This study involved a comprehensive comparison between experimental results and simulations, providing a thorough analysis of the primary factors contributing to experimental discrepancies [12].

Wang and colleagues offer an extensive overview of computational methodologies for predicting hydrodynamic noise. The direct method relies on solving the compressible Navier–Stokes equations (NSE), which provides acoustic results alongside the fluid dynamic solution throughout the computational grid. When employed in tandem with a direct numeric solution (DNS) of the NSE, this method is highly accurate but becomes impractical for most flows in the turbulent regime

due to the substantial increase in computational expenses, particularly as the Reynolds number (R_e) of the flow rises, where it scales as $R_e=3.5x10^5$ in wall-bounded turbulence [13].

Zhang and colleagues employed Lighthill acoustic simulation theory and in conjunction with the FW-H equation to anticipate the flow characteristics and hydrodynamic noise produced by an underwater vehicle. They explored the impact of the stern rudder on hydrodynamic noise and conducted simulations for both cross-type and X-type rudders. The outcomes revealed that X-type rudders had a less pronounced hindrance on the flow field compared to conventional cross-type rudders, and there was a notable enhancement in the hydrodynamic noise performance of X-type stern rudders [14].

In their study, Liu and colleagues investigated the distribution range of hydrodynamic noise stemming from wake shedding. They elucidated the generation mechanism of hydrodynamic noise in underwater vehicles through a combination of experimental measurements and simulations involving scaled models of underwater vehicles [15].

Yeo and colleagues conducted both experimental and numerical investigations into flow-induced noise in submarines during snorkeling operations. They elucidated the respective contributions of bubble noise and turbulence noise to the overall URN from submarines [16].

Bagheri et al. examined the acoustic behavior of the DTMB4119 hull and a four-bladed propeller across different rotational speeds under both cavitating and non-cavitating conditions. Their findings highlighted the substantial influence of cavitation on noise production, offering valuable insights into its contribution to the acoustic profile of marine vessels [17].

Rocca et al. primarily focused on the submarine's inherent configuration, excluding the presence of a propeller, the primary focus of Rocca et al.'s investigation was to emphasize the acoustic characteristics of the hull independently and recreate the condition of silent cruising, characterized by the deactivation of unnecessary noise sources and minimized speed to reduce propeller noise. In this setup, the wake emerges as the primary contributor to noise generation. The results illustrate that the acoustic spectrum exhibits a broad range of frequencies in the far-field region,

while the sound pressure level (SPL) measured in proximity reveals distinctive patterns associated with the presence of the sail and additional structures [18].

It is widely recognized that submarines rely on various appendages that play a crucial role in their hydrodynamic behavior, particularly in terms of turbulence development. Among these appendages, the sails and propellers hold significant importance in shaping the wake flow characteristics. In a recent study by Wang et al. it was highlighted that tail rudders of underwater vehicles have a profound impact on the wake field and flow-induced noise [19].

Numerical simulations provide valuable insights into flow-induced noise generated by structures resembling components of submarines. For instance, Qu et al. investigated the flow field characteristics and hydrodynamic noise of a trapezoidal rudder wing at varying rudder angles through simulation. Their findings revealed that the flow noise exhibits a broad sound pressure level spectrum without any distinct dominant frequency [20].

Kellett and colleagues utilized this method to forecast the underwater noise produced by LNG ships, and the outcomes aligned with experimental data. They conducted numerical simulations to assess the influence of the free surface on the obtained outcomes. Their findings revealed that, for frequencies up to approximately 200 Hz, solutions excluding the free surface component yielded higher levels of sound pressure. Conversely, for frequencies exceeding 200 Hz, the outcomes of solutions with and without a free surface demonstrated comparable results. Consequently, it can be inferred that, for investigations conducted at frequencies above 200 Hz, the consideration of the free surface can be disregarded to mitigate computational expenses [21].

In their study, Abshagen and colleagues investigated the distribution range of hydrodynamic noise originating from wake shedding. They elucidated the mechanism responsible for the generation of hydrodynamic noise in underwater vehicles through a combination of experimental measurements and simulations involving scaled models of underwater vehicles [22].

Ma et al. discovered that the interaction between a submarine's hull and appendages produces inverse pressure gradients during motion. These gradients result in boundary layer separation and the development of complex flow dynamics within

the separation zone, generating a series of eddies, causing intense turbulent pressure fluctuations, and ultimately enhancing the flow noise source [23].

This study shifts the focus from propeller-induced noise, which dominates most existing research in underwater acoustics, to the noise generated by the flow itself. By exploring this less-studied aspect in greater detail, it provides a significant contribution to the field. Understanding the dynamics of flow-induced noise is crucial for developing quieter and more efficient designs for underwater vehicles, particularly in applications such as military operations and environmental monitoring.

2
METHODS

2.1 Fundementals Of Acoustics

In this section, methods related to flow-induced noise are discussed in detail. Definitions of sound and noise, basic quantities of sound, and concepts of noise propagation are explained. Furthermore, acoustic analogies and numerical methods used in hydroacoustic predictions are examined. The Fast Fourier Transform (FFT) method is also described. Finally, the governing equations used in CFD analyses are introduced, emphasizing their importance in analyzing flow-induced noise.

2.1.1 What Is Sound and Noise

The physical phenomenon known as noise is the result of oscillations produced by a vibrating source in air pressure, stimulating the sense of hearing in humans. Noise, on the other hand, is used to refer to unwanted sound or sound pollution. The most basic form of noise is depicted by the harmonic wave.

$$x(t) = A\sin(2\pi fT + \phi) \tag{2.1}$$

- The amplitude (A) determines the magnitude of the oscillation linked to the wave (intensity of the noise).
- The period (T) signifies the duration it takes for the wave to replicate the same oscillation.
- The frequency (f) denotes how many times a particle repeats the same oscillation within a unit of time.
- The phase (ϕ) denotes the displacement of the wave relative to the axis utilized for its analytical depiction.
- The wavelength (λ) represents the distance a particle travels during one period.

2.1.2 Basic Quantities of Sound

The basic quantities related to sound are decibel, sound power level, sound pressure level, and sound intensity level.

2.1.2.1 Decibel

Decibel, a logarithmic and dimensionless unit frequently employed to denote the ratio of a specific reference power or quantity level, particularly in the context of sound intensity. The decibel consistently serves as a measure of the relationship between two values, often maintaining the same value despite variations in the measured power. One bel signifies a ratio of 10 between two magnitudes. The more prevalent unit, decibel, is defined as 10 times the logarithm of the ratio. The term "level" is applied to magnitudes quantified in decibels. To illustrate, the level of a pressure value P concerning the reference value P_0 is expressed in decibels as the logarithmic ratio of P to P_0 multiplied by 10 [1], [24].

$$Level\ (dB) = 10 \log\left(\frac{P}{P_0}\right) \tag{2.2}$$

2.1.2.2 Sound Power Level

Sound power is defined as the energy power of the sound emitted by a source, and its magnitude is denoted as the sound power level (L_w). In acoustic calculations, the source's sound power level is a standard measure. The expression for the sound power level (L_w) of a source with a sound power of W is given by equation (2.3) [1], [24].

$$L_w = 10 \log\left(\frac{W}{10^{-12}}\right) \tag{2.3}$$

2.1.2.3 Sound Pressure Level

The pressure at a point is quantified in terms of levels by logarithmically comparing it to reference (P_0) value [1].

$$SPL = 20 \log\left(\frac{p}{p_0}\right) \tag{2.4}$$

Here, P is the the measured sound pressure level, and P_0 is the internationally accepted reference pressure. This value is taken as 20 μPa ($2x10^{-5}$ N/m^2) for

aeroacoustics and 1 μPa ($1x10^{-6}$ N/m^2) for hydroacoustics. SPL is quantified in decibels (dB).

SPL is a logarithmic measure of sound power or intensity, meaning that as the sound pressure increases, SPL also increases, but due to the logarithmic nature, a 10-fold increase in sound pressure only results in a 20 dB increase.

2.1.2.4 Sound Intensity Level

The pressure at a point is quantified in terms of levels by logarithmically comparing it to reference (P_0) value [1].

$$IL = 10 \log\left(\frac{I}{I_0}\right) \tag{2.5}$$

2.1.3 Sound Propagation

Sound can spread through three main mechanisms:

- Airborne transmission: Vibrating surfaces of an object generate pressure waves in the air, causing sound to travel through the air.
- Air and structure transmission: Pressure oscillations force other surfaces to vibrate, creating new sources of sound. For instance, engine noise can find alternative paths by vibrating the vehicle cabin and panel walls.
- Structure-borne transmission: Vibrating sources induce vibrations in connected elements, and sound spreads from the surfaces of these elements. Employing suitable engine mounts can help reduce the transmission of noise through the structure.

The speed of sound varies depending on the environment. Specifically, sound propagation underwater is influenced by factors such as salinity, depth, temperature, and pressure. While the speed of sound in air at 15°C is approximately 340 m/s, the speed of sound underwater is typically around 1500 m/s.

2.1.4 Elementary Acoustics Sources

The industrial applications encompass various potential acoustic sources, each with distinct characteristics. However, the noise emanating from most of these sources can be conceptualized as that produced by elementary sources or a combination thereof.

The acoustic sources vary in terms of the physical processes generating noise, their shapes, noise directivity, the modeling equations used to describe their characteristics, and their intensity.

2.1.4.1 Monopole

A monopole, the most basic acoustic source, is depicted as a spherical source that generates a spherical wave in the surrounding free space through its pulsation.

In practical terms, any sound source with dimensions significantly smaller than the wavelength of the radiated sound will function as a monopole, effectively emitting sound in all directions [25].

2.1.4.2 Dipole

A dipole is an acoustic source consisting of two monopoles situated close to each other, pulsating with equal strength and a phase shift of 180 degrees.

The oscillation out of phase between the two monopoles leads to the creation of a net fluctuating force along the axis that separates them. The pressure radiation produced is dependent on the radius (r) and the polar angle (θ).

In industrial applications, a monopole situated near a rigid reflecting surface acts as a dipole because, at a distance from the source, its emission can be perceived as the combination of two waves i.e., the direct wave and the reflected one (with a phase shift) [26].

2.1.4.3 Quadrapole

As a dipole is characterized by the combination of two monopoles oscillating out of phase, a quadrupole is defined as an acoustic source consisting of two dipoles close to each other and oscillating with a 180-degree phase-shift. While a dipole has one axis, the quadrupole has two.

Two types of quadrupoles (lateral and longitudinal) can be obtained based on the arrangement of the dipoles. In both cases, their acoustic power can be compared to the one emitted by a monopole, and the following relationship holds.

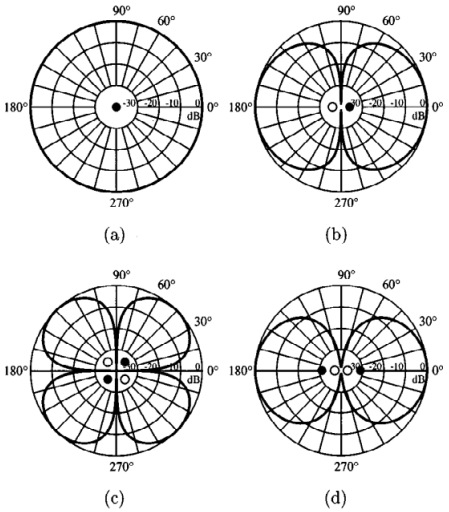

Figure 2.1 Theoretical directivity patterns for far-field sound pressure levels radiated from (a) monopole, (b) dipole, (c) lateral quadrupole, and (d) longitudinal quadrupole sound sources[25].

Figure 2.1 illustrates the theoretical directivity patterns of far-field sound pressure levels for monopole, dipole, lateral quadrupole, and longitudinal quadrupole sound sources.

2.2 Acoustics Analogies

Aero-acoustic science originated in 1952 with the development of the first aero-acoustical theory by Lighthill [3], [4], focusing on unbounded fluctuating flows in a uniform medium. Subsequently, numerous studies have been undertaken, incorporating enhancements and extensions suggested by Curle [27] in 1955, which accounted for the impact of fixed solid boundaries. Powell [28] and Howe [29] further contributed in 1960 and 1975, respectively, by separating the effects of vorticity and mean flow on the acoustic wave. Ffowcs Williams-Hawkings [5] in 1969 expanded Curle's exploration to include moving bodies.

The term "acoustic analogy" denotes a method for describing acoustic propagation through an equation featuring a wave operator on the left-hand side and other terms on the right-hand side treated as an acoustically equivalent source term. The notion of analogy can be applied to any field of study when its fundamental equation is expressed with an equivalent source term. In acoustics, the physics of wave propagation in a uniform stagnant fluid is articulated by the wave equation.

$$\frac{\partial^2 \rho'}{\partial t^2} - c_0^2 \nabla^2 \rho' = 0 \tag{2.6}$$

where ρ' denotes the density fluctuations and c_0 is the speed of sound in standard conditions. For an isentropic flow, $c_0^2 = \frac{\partial p}{\partial \rho}$, which, in the case of a stagnant fluid,

$$c_0^2 = \frac{p'}{\rho'} \tag{2.7}$$

The outcome $p'(x,t)$ obtained from equations (2.6) signifies the density fluctuations in both space and time. In a uniform and motionless fluid, the receiver (the point where the noise is computed) exhibits identical pressure p_0, density ρ_0 , and speed of sound c_0 at any spatial location and moment in time [30]. Any deviation from these conditions (in a non-uniform medium) introduces additional terms in equation (2.6). The term "acoustic analogy" becomes applicable when all these additional terms are consolidated on the right-hand side. For the receiver, these terms are treated as an equivalent acoustic source emitting noise in a uniform fluid.

2.2.1 Lighthill Acoustic Model

The initial and renowned acoustic analogy, developed by Lighthill [3], focuses on describing the density fluctuations in a uniformly stagnant medium. The transmission of sound in a homogeneous medium, devoid of material sources or external forces, is elucidated by the equations;

$$\frac{\partial \rho}{\partial t} + \frac{\partial \rho u_i}{\partial x_i} = 0 \tag{2.8}$$

$$\frac{\partial (\rho u_i)}{\partial t} + \frac{\partial \left(\rho u_i u_j + p_{ij}\right)}{\partial x_i} = 0 \tag{2.9}$$

Here, ρ represents the density, u_i and u_j denote the velocity components, and p_{ij} corresponds to the stress tensor.

$$p_{ij} = -\sigma_{ij} + (\rho - \rho_0)\delta_{ij} \tag{2.10}$$

The term p represents the thermodynamic pressure of the flow field, δ denotes the Kronecker delta, and σ_{ij} refers to the viscous stress tensor.

$$\sigma_{ij} = \mu(\frac{\partial u_i}{\partial x_j} + \frac{\partial u_j}{\partial x_i} - \frac{2}{3}\frac{\partial u_i}{\partial x_i}\delta_{ij}) \tag{2.11}$$

Taking the time derivative of equation (2.8) and combining it with the divergence of equation (2.9), the following expression is obtained:

$$\frac{\partial^2 \rho}{\partial t^2} - c_0^2(\nabla^2 \rho) = \frac{\partial^2 T_{ij}}{(\partial x_i)(\partial x_j)} \tag{2.12}$$

T_{ij} represents the Lighthill turbulence stress tensor, which can be expanded as follows:

$$T_{ij} = \rho u_i u_j + P_{ij} - c_0^2(\rho - \rho_0) - \delta_{ij} \tag{2.13}$$

If equation (2.8) is substituted into equation (2.11) and simplified, the following expression is obtained:

$$T_{ij} = \rho u_i u_j - \sigma_{ij} + \delta_{ij}[(p - p_0) - c_0^2(p - p_0) \tag{2.14}$$

In this context, $\rho u_i u_j$ refers to the time-dependent propagation of the flow or Reynolds stress, σ_{ij} represents the noise induced by shear forces, and $\delta_{ij}(p - c_0^2\rho)$ captures the nonlinear contributions to noise formation.

In laminar flows, the stress tensor is as shown in equation (2.11), while in turbulent flows, the stress tensor is as follows:

$$\sigma_{ij} = \sigma_{ij,lam} + \sigma_{ij,turb} = \mu_{eff}(\frac{\partial u_i}{\partial x_j} + \frac{\partial u_j}{\partial x_i} - \frac{2}{3}\frac{\partial u_i}{\partial x_i}\delta_{ij}) \tag{2.15}$$

$$\mu_{eff} = \mu_{lam} + \mu_{turb} \tag{2.16}$$

In potential flows, the stress tensor is given by $\sigma_{ij} = 0$.

2.2.2 Ffowcs Williams Hawkings Acoustic Model

The FW-H equation is derived from the continuity equation and the Navier-Stokes equations, representing an inhomogeneous wave equation.

The FW-H equation, stemming from the principles of momentum and mass conservation, extends Lighthill's acoustic analogy to account for the impacts of surfaces undergoing arbitrary motions.

$$\frac{1}{a_0^2}\frac{\partial^2 p'}{\partial t^2} - \nabla^2 p' = \frac{\partial^2}{\partial x_i \partial x_j}\{T_{ij}H(f)\} - \frac{\partial}{\partial t}\{[P_{ij}n_j + \rho u_i(u_n - v_n)]\delta(f)\} + \frac{\partial}{\partial t}\{[\rho_0 v_n + \rho(u_n - v_n)]\delta(f)\} \quad (2.17)$$

Where;

u_i is the fluid velocity in the direction of x_i

u_n is fluid velocity normal to the surface (f=0)

v_i is surface velocity in the direction of x_i

v_n is surface velocity perpendicular to the surface

$\delta(f)$ is Dirac delta function

$H(f)$ is the Heaviside function

P' denotes the acoustic pressure in the distant field (P' = P - P_0). The mathematical surface represented by f = 0 is introduced to encapsulate the external flow problem (f > 0) within an unbounded spatial context. This introduction enables the utilization of generalized function theory and the free-space Green function for problem resolution. The surface defined by f = 0 serves as the source surface and can either impermeable surface or be situated as a permeable surface away from the body. The unit normal vector, denoted as n_i, points towards the external region (f > 0), a_0 represents the far-field sound speed, and T_{ij} represents the Lighthill stress tensor, as defined by [31],

$$T_{ij} = \rho u_i u_j + P_{ij} - a_0^2(\rho - \rho_0) - \delta_{ij} \quad (2.18)$$

P_{ij} is the compressive stress tensor, and for a Stokesian fluid, its expression is given by;

$$P_{ij} = \mathrm{p}\delta_{ij} - \mu\left[\frac{\partial u_i}{\partial x_j} + \frac{\partial u_j}{\partial x_i} - \frac{2}{3}\frac{\partial u_k}{\partial x_k}\delta_{ij}\right] \tag{2.19}$$

The free-stream quantities are represented by the subscript "0"

The solution to equation (2.11) utilizes the free-space Green's function ($\frac{\delta(g)}{4\pi r}$). The comprehensive solution involves both surface and volume integrals. In this context, the surface integral considers the impacts of monopole, dipole, and certain quadrupole sources, while the volume integral exclusively addresses quadrupole sources situated outside the source surface. Under conditions of low subsonic velocity, the volume integral's contribution diminishes significantly, and the source surface effectively encompasses the source region. Consequently, the volume integral is disregarded, leading to the following expression [31]:

$$\mathrm{p}'(\vec{x},\mathrm{t}) = \mathrm{p}'_{\mathrm{T}}(\vec{x},\mathrm{t}) + \mathrm{p}'_{\mathrm{L}}(\vec{x},\mathrm{t}) \tag{2.20}$$

Where,

$$4\pi\mathrm{p}'_{\mathrm{T}}(\vec{x},\mathrm{t}) = \int_{f=0}\left[\frac{\rho_0\left(\dot{U}_n + U_{\dot{n}}\right)}{r(1-M_r)^2}\right]dS + \int_{f=0}\left[\frac{\rho_0 U_n\left\{r\left(M_r + \dot{a}_{0(M_r-M^2)}\right)\right\}}{r^2(1-M_r)^3}\right]d \tag{2.21}$$

$$4\pi\mathrm{p}'_{\mathrm{L}}(\vec{x},\mathrm{t}) = \frac{1}{\mathrm{a}_0}\int_{f=0}\left[\frac{\left(\dot{\mathrm{L}}_{\mathrm{r}}\right)}{r(1-M_r)^2}\right]dS + \int_{f=0}\left[\frac{(L_r - L_M)}{r^2\,(1-M_r)^2}\right]dS + \frac{1}{\mathrm{a}_0}\int_{f=0}\left[\frac{L_r\left\{\left(\mathrm{r}\dot{\mathrm{M}}_{\mathrm{r}}\right) + a_0(M_r - M^2)\right\}}{r^2(1-M_r)^3}\right]dS \tag{2.22}$$

$$U_i = v_{\mathrm{i}} + \frac{\rho}{\rho_0(u_i - v_{\mathrm{i}})} \tag{2.23}$$

$$L_i = \mathrm{P}_{\mathrm{ij}}\hat{n_j} + \rho u_i(u_n - v_n) \tag{2.24}$$

When the integration surface aligns with a closed, impenetrable wall, the terms in equation (2.15) and (2.16) represented by ($p'_T(\vec{x}, t)$) and ($p'_L(\vec{x}, t)$) are referred to as the thickness noise term and loading noise term, respectively [31].

The expressions within brackets in equation (2.15) and (2.16) indicate that the integral kernel is evaluated at the retarded time step (τ), where t represents time and r is the distance to the receiver, expressed as follows:

$$\tau = t - \frac{r}{a_0} \tag{2.25}$$

In addition to these, the terms with subscripts featured in the formulas represent elements of vectors, where subscripts denote unit vectors.

For instance, $L_r = \vec{L}.\ \hat{\vec{r}} = L_i r_i$ and $U_n = \vec{U}.\vec{n} = U_i n_i$, $\hat{\vec{r}}$ and $\vec{n}$ correspond to unit vectors in the radiation and wall-normal directions, respectively. The dot (.) placed on a variable signifies the source-time derivative of that variable [31].

2.3 Numerical Methods Used in Hydroacoustic Predictions

Computational Aeroacoustics is a discipline rooted in CFD methods, focusing on modeling flow-induced noise and its interactions within the flow field. CAA methodologies are broadly categorized into two main approaches: Direct Numerical Simulation (DNS) and Hybrid Methods.

DNS involves solving the Navier-Stokes equations numerically without employing any turbulence models. This method requires resolving all turbulence scales within the flow, capturing even the smallest eddies. The primary advantage of DNS is its ability to directly solve both the flow and noise fields with high accuracy. This makes it particularly effective for low Reynolds number flows and geometrically simple configurations. However, the computational cost and complexity associated with DNS are prohibitively high, especially for high Reynolds number flows, where the sheer number of scales to resolve becomes unmanageable. Consequently, DNS is largely confined to academic studies or specific, simplified cases.

Hybrid approaches play a critical role in CAA studies by enabling the decoupling of flow and acoustic field computations, leading to increased computational efficiency and versatility. In the hybrid method utilized, the flow field was solved

using Navier-Stokes equations, and the results were subsequently applied to acoustic calculations. This two-step process allowed for a clear distinction between hydrodynamic and acoustic phenomena, making it particularly suitable for analyzing complex geometries such as submarines.

The separation of currents and the formation of vortices are the main causes of noise created by currents, and they need to be studied carefully. These processes happen when the flow of water detaches from a surface and creates swirling motions, which increase noise levels. Understanding these effects is important for reducing noise, especially in things like underwater vehicles, ships, and other marine structures.

Once the flow around the submarine was resolved to the desired level of accuracy, the flow-induced noise was calculated using the FW-H method. To perform these calculations, the solution was conducted in a transient manner to capture the instantaneous pressure, velocity, and density fields required for the FW-H formulation. This comprehensive approach ensured the accurate prediction of both the flow characteristics and their associated noise generation, providing valuable insights into the acoustic signature of the submarine while maintaining hydrodynamic performance.

When the flow-induced noise was calculated using the FW-H method, further analysis was necessary to understand the frequency characteristics of the acoustic signature. The temporal data obtained from the simulation provided insights into the instantaneous pressure fluctuations; however, identifying dominant frequencies and spectral components required transforming this data from the time domain to the frequency domain.

This transformation is critical in computational aeroacoustic studies, particularly for submarine noise prediction, where the interaction between flow dynamics and acoustic properties must be analyzed in detail. The frequency analysis helps isolate specific acoustic features and determine how various flow structures contribute to noise generation. This step forms the basis for optimizing design parameters to minimize acoustic signatures while maintaining hydrodynamic performance.

2.4 Fast Fourier Transform (FFT)

In computational aeroacoustic analyses aimed at predicting the acoustic performance of submarines, data recorded by receivers during the analysis must be transformed from the time domain to the frequency domain using appropriate signal processing techniques. The Fast Fourier Transform is a mathematical method that facilitates this transformation, converting time-dependent data into the frequency domain. FFT identifies periodic components within complex signals, disregarding non-repeating signals, and decomposes them into harmonic components. The discretization of collected signals during analysis is achieved using suitable filtering techniques. Essentially, with the assistance of an amplitude function and an appropriate window function (e.g., Hanning, Hamming), the data are effectively transferred into the frequency domain.

The data collected from the receivers positioned in Figure 3.5 were processed using FFT, converting the time-domain signals into the frequency domain. This transformation allowed for a detailed frequency analysis, enabling the identification of specific acoustic features and spectral components of the signals, which are essential for understanding the acoustic performance of the submarine.

2.5 Governing Equations in Computational Fluid Dynamics

The fundamental equations in fluid mechanics problems can be formulated in differential form, and solving these equations analytically is highly challenging. Depending on the chosen theory and method, solutions to these equations can be obtained by introducing certain simplifications.

2.5.1 Continuity Equation

The conservation of mass, commonly referred to as the continuity equation, is expressed as follows:

$$\frac{\partial \rho}{\partial t} + \nabla . \left(\rho \vec{V}\right) = 0 \tag{2.26}$$

In the case of incompressible flow, the equation transforms as follows,

$$\frac{\partial \rho}{\partial t} + \nabla \rho . \vec{V} = 0 \tag{2.27}$$

In the scenario of steady flow, the equation transforms as follows,

$$\nabla . \left(\rho \vec{V}\right) = 0 \tag{2.28}$$

If the flow is both incompressible and steady the equation transforms as follows

$$\nabla . \vec{V} = 0 \tag{2.29}$$

In situations where the flow is incompressible and unsteady, the resolution of the equation results in a distinct outcome.

2.5.2 Conservation of Momentum

The conservation of momentum equation is as follows

$$\frac{\partial}{\partial t}(\rho . \vec{V} + \nabla \rho . \vec{V}\vec{V}) = - \nabla P + \nabla (\vec{\tau}) + \rho . \vec{g} + \vec{F} \tag{2.30}$$

Here, p is static pressure, $\vec{\tau}$ is the stress tensor, g represents gravitational force, ρ is density, and F denotes external body forces. The stress tensor is provided as follows.

$$\vec{\vec{\tau}} = \mu \left[\left(\nabla \vec{V} + \nabla \overrightarrow{V^T} \right) - \frac{2}{3} \nabla \vec{V} I \right] \tag{2.31}$$

Here, μ is the molecular viscosity, and I is the unit tensor.

Given the assumption of incompressibility for both fluids, with constant density and a continuous velocity field the momentum equation, also known as the Navier-Stokes equation, for the incompressible two-phase flow considering the assumptions can be formulated as follows:

$$\frac{\partial U}{\partial t} + \frac{\partial \left(U_i U_j\right)}{\partial x_j} = -\frac{1}{\rho} * \frac{\partial P}{\partial x_i} + \frac{\partial}{\partial x_j} \left[\upsilon \left(\frac{\partial U_i}{\partial x_j} + \frac{\partial U_j}{\partial x_i} \right) \right] - \frac{\partial \overline{\left(u'_\iota u'_j\right)}}{\partial x_j} \tag{2.32}$$

In the given equation, u_i and u_i' represent the mean and fluctuation velocity components along the cartesian coordinate x_i, respectively. P represents the mean pressure, ρ denotes the density, and ν represents the kinematic viscosity.

2.5.3 Fundamental Equations of Underwater Acoustics

Underwater acoustics relies on fundamental equations to describe the physical behavior of sound waves propagating through water. These equations are derived from the basic principles of fluid mechanics and wave theory, explaining the generation, propagation, and interactions of sound waves in a fluid medium. The wave equation, derived from the continuity and momentum equations, is particularly vital for characterizing the temporal and spatial behavior of sound in underwater environments.

If the time derivative of the linearized continuity equation and the spatial derivative of the linearized momentum equation are taken, the resulting equations are obtained as follows:

$$\frac{\partial^2 \rho}{\partial t^2} + + \frac{\partial}{\partial x_i}(\rho_0 \frac{\partial u_i}{\partial t}) \tag{2.33}$$

$$\frac{\partial}{\partial x_i}\left(\rho_0 \frac{\partial u_i}{\partial t}\right) + \frac{\partial^2 p}{\partial x^2} = 0 \tag{2.34}$$

From these equations, the linear acoustic wave equation is derived by substituting the components of density variation. Here, p represents the acoustic pressure.

$$\frac{\partial^2 p}{\partial {x_i}^2} - \frac{1}{c^2}\frac{\partial^2 \rho}{\partial t^2} = 0 \tag{2.35}$$

For example, the one-dimensional linear wave equation is expressed as follows:

$$\frac{\partial^2 y}{\partial x^2} = \frac{1}{c^2}\frac{\partial^2 y}{\partial t^2} \tag{2.36}$$

The expression for the speed of sound in the equation is given as:

$$c^2 = \frac{T}{\rho_L} \tag{2.37}$$

In the given expression, T refers to the linear tensile force measured in newtons (N), whereas ρ_L represents the linear mass density measured in kilograms per meter (kg/m) [32].

2.5.4 Modeling of Free Water Surface

The Volume of Fluid (VOF) model is a multiphase simulation method ideal for analyzing flows of multiple immiscible fluids, utilizing numerical grids that precisely define the interfaces between the mixture's phases [33]. The volume fraction is determined by the following equation:

$$\frac{\partial a}{\partial t} + u_i \frac{\partial a}{\partial x_i} = 0 \tag{2.38}$$

In this formulation, u_i refers to the fluid velocity, and α indicates the fluid fraction within each cell. If α = 1, the cell is entirely filled with water; if α = 0, the cell is completely filled with air; and when α = 0.5 α=0.5, the cell contains an equal mix of 50% water and 50% air.

2.5.5 Modeling of Turbulence

The majority of engineering-relevant fluid flows exhibit irregularly fluctuating flow quantities. Frequently, these fluctuations occur at small scales and high frequencies, making their accurate resolution in time and space computationally prohibitive. Rather than pursuing the solution of the exact governing equations through DNS for turbulent flows, a more cost effective approach involves solving for averaged or filtered quantities to approximate the influence of small fluctuating structures. Turbulence models provide various methodologies for modeling these structures.

2.5.5.1 k-ε Turbulence Model

The realizable k-epsilon turbulence model, introduced by Shih et al. [34], is a two-equation model. It requires solving transport equations for turbulent kinetic energy (k) and turbulent dissipation rate (ε) to ascertain the turbulent eddy viscosity (μ_t) [29]. Turbulent kinetic energy (k) for incompressible, steady flows (standard k-ε model) is expressed as follows:

$$\rho \frac{\partial k}{\partial t} + \rho u_j \frac{\partial k}{\partial x_j} = \tau_{ij} \frac{\partial u_i}{\partial x_j} - \rho \varepsilon + \frac{\partial}{\partial x_j}\left[\left(\mu + \frac{\mu_t}{\sigma_k}\right)\left(\frac{\partial k}{\partial x_j}\right)\right] \tag{2.39}$$

The rate of turbulent kinetic energy dissipation (ε) is expressed as follows:

$$\rho \frac{\partial \varepsilon}{\partial t} + \rho u_j \frac{\partial \varepsilon}{\partial x_j} = C_{\varepsilon 1} \frac{\varepsilon}{k} \tau_{ij} \frac{\partial u_i}{\partial x_j} - C_{\varepsilon 2} \frac{\varepsilon^2}{k} + \frac{\partial}{\partial x_j}\left[\left(\mu + \frac{\mu_t}{\sigma_\varepsilon}\right)\frac{\partial \varepsilon}{\partial x_j}\right] \tag{2.40}$$

Kinematic eddy viscosity:

$$\mu_t = \rho C_\mu \frac{k^2}{\varepsilon} \tag{2.41}$$

Closure coefficients and Auxiliary Relations:

$$C_{\varepsilon 1} = 1.44,\ \ C_{\varepsilon 2} = 1.92,\ \ C_\mu = 0.09,\ \ \ \sigma_k = 1.0,\ \ \sigma_\varepsilon = 1.3 \tag{2.42}$$

$$\omega = \frac{\varepsilon}{C_\mu k} \quad and \quad l = \frac{C_\mu k^{3/2}}{\varepsilon}$$

3
NUMERICAL ANALAYSES OF DARPA SUBMARINE

In this chapter, the DARPA Suboff AFF-8 model was examined under fully submerged conditions with multiple grid resolutions. A verification study was carried out to determine the most suitable grid size. The numerical method was then validated by comparing its results with existing experimental data using the selected grid. After validation, simulations were performed at varying depths and speeds to assess how these factors influence the submarine's hydroacoustic behavior.

3.1 Geometric Characteristics of Darpa Suboff AFF-8 Model

The DARPA Suboff submarine model, designed by the Defense Advanced Research Projects Agency (DARPA), is a well-established benchmark in ship hydrodynamics research. This thesis utilizes the Suboff model to perform CFD resistance analyses and acoustic assessments. The model is available in two configurations: the AFF-1, representing the bare hull without appendages, and the AFF-8, which includes a sail and four stern rudder fins. In this study, the AFF-8 configuration, featuring the complete set of appendages, is selected. Figure 3.1 illustrates the 3D geometry of the model at a scale of $\lambda = 24$, with the key dimensions summarized in Table 3.1.

Figure 3.1 Darpa Aff-8 geometry from side view

Table 3.1 Main dimensions of the DARPA AFF-8 submarine model

	Symbol	AFF8
Geometric scale ratio	λ	24
Length over all	L_{OA} [m]	4.356
Length between perpendicular	L_{BP} [m]	4.261
Maximum diameter	D_{MAX} [m]	0.508
Wetted surface area	A_W [m^2]	6.348
Displacement	∇ [m^3]	0.706

3.2 Computational Domain and Boundary Conditions

In CFD simulations, the application of appropriate initial and boundary conditions is crucial for achieving an accurate approximation of the solution and reliable analysis of the flow around the geometry. The computations are performed within a cartesian coordinate system, with the origin positioned at the submarine's stern along the vertical plane. In this setup, the negative x-axis represents the direction of the flow, while the positive z-axis corresponds to the upward direction.

For the resistance analyses, a rectangular computational domain was established to simulate the flow around the submarine. The dimensions of this domain were defined following the guidelines of the International Towing Tank Conference (ITTC) [35]. Adhering to these guidelines is essential to ensure that the numerical simulations yield accurate and reliable results.

The hull surface is treated as a no-slip wall, while the inlet, top, bottom, and far-field boundaries are defined as velocity inlets with an initial zero-velocity condition. The outlet is modeled as a pressure outlet. The simulations employ a flat

VOF wave at varying speeds, with the computational domain encompassing the entire flow field to prevent surface distortions and ensure solution stability.

In the resistance analyses, the submarine model remained fixed while resistance values were calculated by introducing flow through the velocity inlet based on the velocity range specified in the experimental conditions.

The control volume is box-shaped, with a height and width of 2.0 LPP. The inlet boundary is positioned 1.5 LPP upstream of the submarine's bow, while the outlet boundary extends 5.0 LPP downstream from the stern. Figure 3.2 present the dimensions of the computational domain and the specifics of the applied boundary conditions.

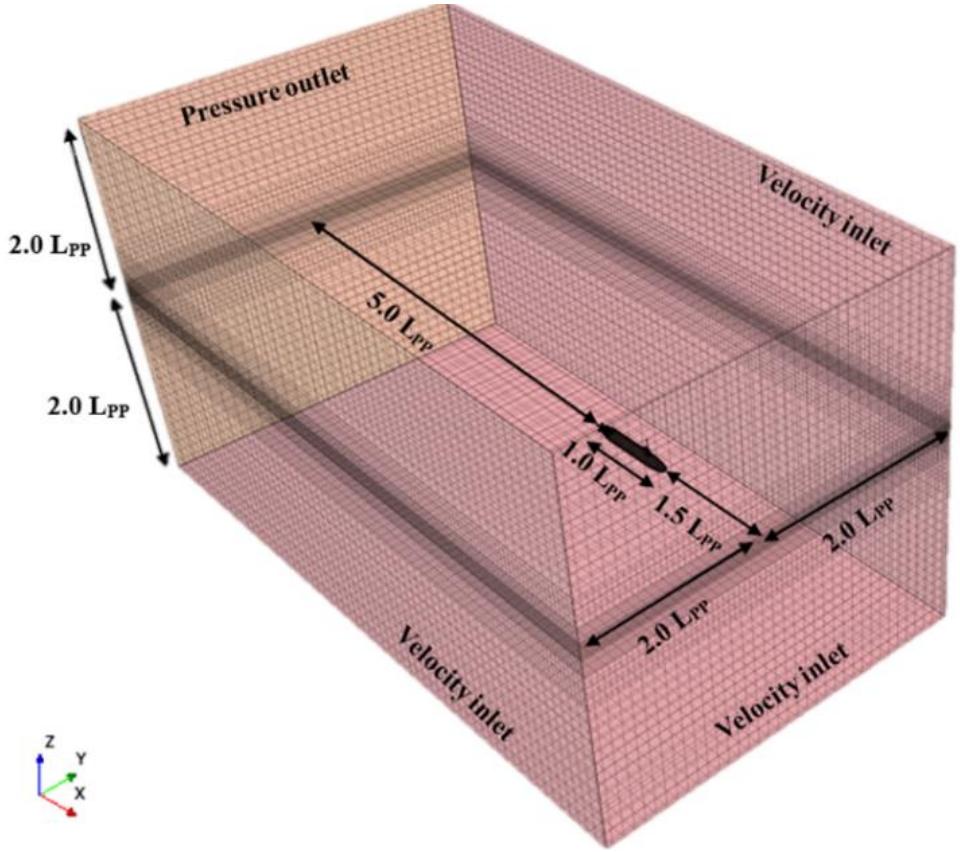

Figure 3.2 Computational domain and the boundary conditions of the simulation

3.3 Mesh Generation

The establishment of an appropriate mesh structure is critical for achieving high accuracy in CFD hydrodynamic analyses. Following the finite volume method, the computational domain is discretized using three-dimensional elements. For the simulations, a trimmer mesh algorithm employing hexahedral elements is utilized throughout the computational domain. In regions of interest, such as the submarine's path and around appendages (rudder fins and sail), mesh refinements are applied to accurately capture potential flow separations and high velocity gradients. Figure 3.3 shows the detailed grid structure used in the simulations.

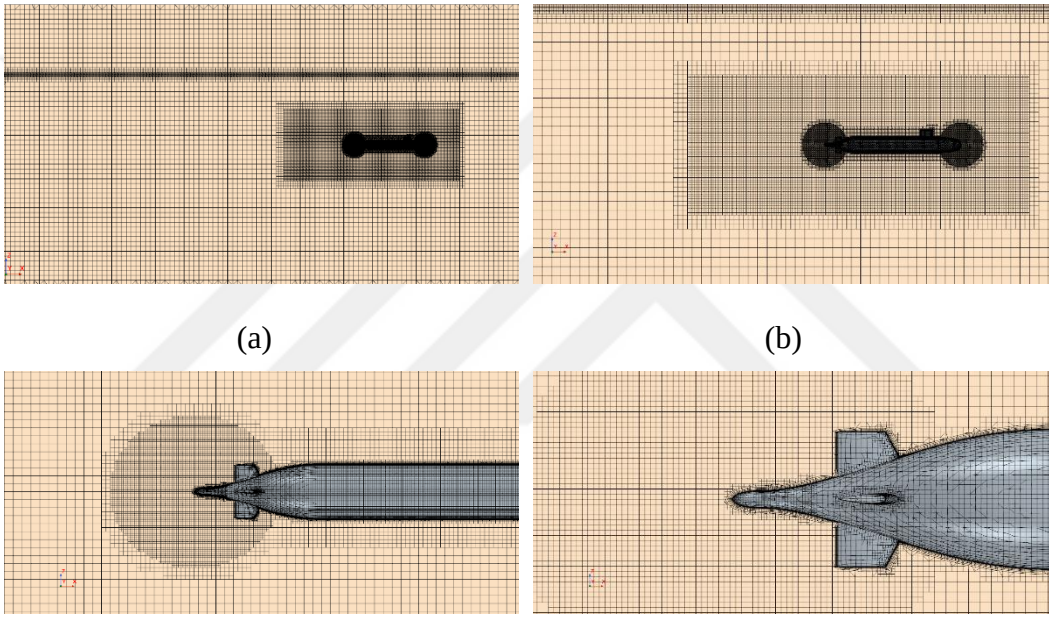

(a) (b)

(c) (d)

Figure 3.3 Grid structure around Darpa; a, b, c represent whole domain ; d is boundary layer grids details

Prism layers are incorporated near the submarine hull enhance the representation of the boundary layer. To satisfy the requirements of the wall function approach, the dimensionless wall distance values are maintained within the range of $30 < y^{+} < 300$.

$$y^{+} = \frac{u_{\tau} * y}{\nu} \tag{3.1}$$

Here, u_{τ} represents the friction velocity, y^{+}denotes the height of the first cell adjacent to the wall, and ν indicates the kinematic viscosity of the fluid. The mesh size and growth rate on the submarine surface were carefully calibrated to maintain

the wall y^+ values within the specified range, ensuring that viscous effects near the submarine were accurately captured. Figure 3.4 illustrates the distribution of wall y^+ values on the DARPA Suboff submarine. As illustrated in the figure, the y+ values are maintained within the target range ($30 < y^+ < 300$).

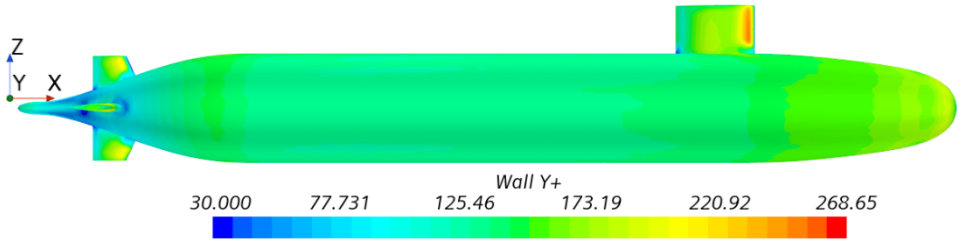

Figure 3.4 Wall y^+ distribution on the DARPA Suboff submarine for Fr = 0.7869

3.4 Physics Modelling

In this thesis, the governing equations, specifically the URANS equations, are discretized using the finite volume method with the commercial CFD software Simcenter Star CCM+. The turbulent flow around the DARPA Suboff submarine model is addressed using the two-layer all $y+$ treatment in conjunction with the realizable k-ε turbulence model, both of which are commonly employed in ship hydrodynamics applications. A second-order scheme is applied for spatial and temporal discretization. To solve the pressure field, the SIMPLE (Semi-Implicit Method for Pressure-Linked Equations) solution algorithm, which facilitates pressure-velocity coupling, is utilized.

The analyses conducted as part of this thesis were executed in a time-dependent (unsteady) manner. For unsteady simulations, choosing an appropriate time step is crucial for ensuring accurate temporal analysis. As per ITTC guidelines [35], a time step of $\Delta t = 0.005-(0.01L/U)$ is recommended for calm water resistance, where L denotes the ship's length and U represents its speed. In this study, a time step of $\Delta t = 0.01$ seconds was implemented. In addition to the ITTC method for determining the time step, it is essential to verify that the Courant-Friedrichs-Lewy (CFL) condition is satisfied. The CFL number is calculated for each solution mesh and must be less than or equal to 1 to ensure numerical stability. It is defined as $CFL=((U*\Delta t)/\Delta x)$, Δt is the time step and Δx represents the size of the smallest mesh element in the computational domain.

3.5 Measurement Locations and Analysis Scenarios

The hull, fin, and sail surfaces were designated as noise sources, with seven receivers positioned as depicted in the image below.

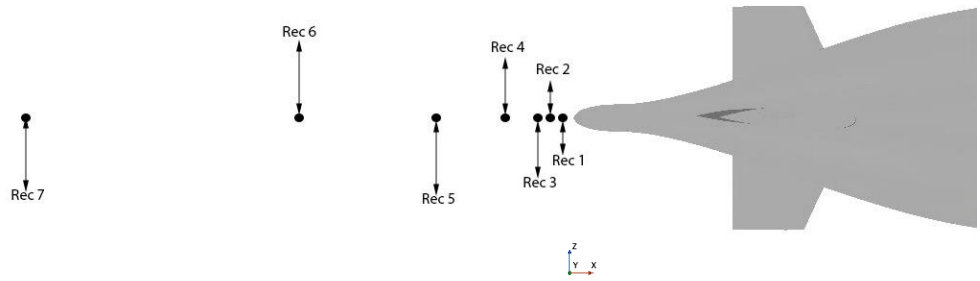

Figure 3.5 Receiver placements positioned aft of the DARPA AFF-8 submarine

The detailed locations of the receivers are presented in Table 3.2.

Table 3.2 Receiver locations

Reciever	Location
1	0.05*D
2	0.1*D
3	0.15*D
4	0.3*D
5	0.6*D
6	1.2*D
7	2.4*D

In these analyses, the submarine's stern point was set as the reference, with depth measured as the vertical distance from this point to the free water surface. The DARPA model was placed at four specific depths beneath the free water surface (L/8, L/4, L, and 4L). Furthermore, five velocities were evaluated at each depth. The various depth positions are illustrated in Figure 3.6.

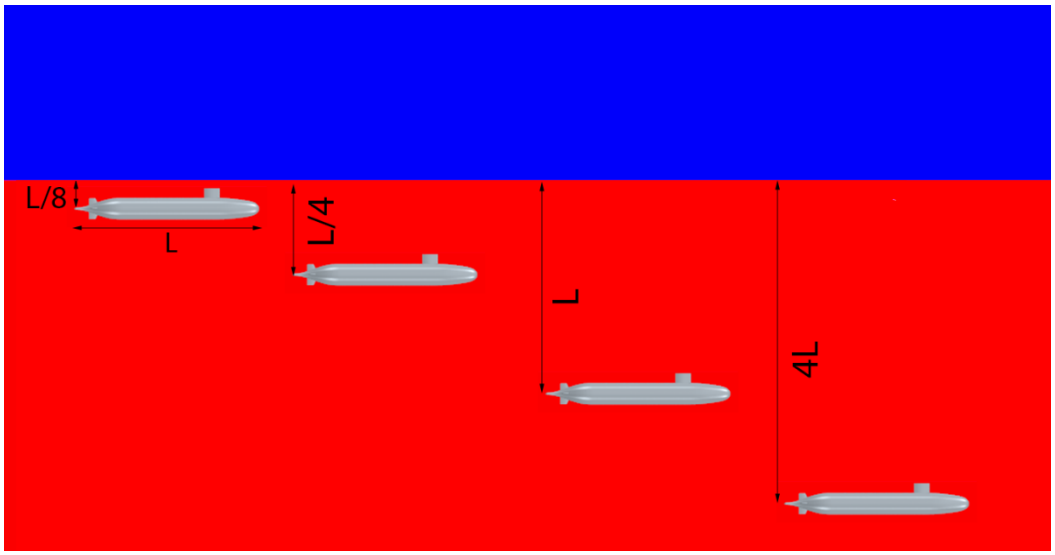

Figure 3.6 The submarine positions shown are illustrative and not to scale.

The depth, velocity, Froude number (Fr), depth Froude number (Fr_h), and Reynolds number (Re) values from the analysis are presented in detail in Table 3.3.

$$Fr = \frac{v}{\sqrt{g * L}}, \qquad Fr_h = \frac{v}{\sqrt{g * D}} \tag{3.2}$$

Froude number (Fr), depth Froude number (Fr_h) formula used in the calculations are given in equation (3.2).

Table 3.3 Conditions of analysis in terms of depth and velocity

Depth	**Velocity (m/s)**	**Fr**	**$Fr_{,h}$**	**Re**
L/8	3.051	0.467	1.320	1.49E+07
	5.144	0.787	2.226	2.52E+07
	6.096	0.933	2.638	2.98E+07
	7.16	1.095	3.098	3.50E+07
	8.23	1.259	3.561	4.02E+07

Table 3.3 Conditions of analysis in terms of depth and velocity (continued…)

Depth	Velocity (m/s)	Fr	$Fr_{,h}$	Re
L/4	3.051	0.467	0.933	1.49E+07
	5.144	0.787	1.574	2.52E+07
	6.096	0.933	1.865	2.98E+07
	7.16	1.095	2.191	3.50E+07
	8.23	1.259	2.518	4.02E+07
L	3.051	0.467	0.467	1.49E+07
	5.144	0.787	0.787	2.52E+07
	6.096	0.933	0.933	2.98E+07
	7.16	1.095	1.095	3.50E+07
	8.23	1.259	1.259	4.02E+07
4L	3.051	0.467	0.233	1.49E+07
	5.144	0.787	0.393	2.52E+07
	6.096	0.933	0.466	2.98E+07
	7.16	1.095	0.548	3.50E+07
	8.23	1.259	0.629	4.02E+07

4
RESULTS

In this section, we present the hydrodynamic results obtained from the simulations. The focus will first be on validating and verifying the numerical model to ensure accuracy and reliability. This will include a detailed examination of mesh dependency, where we analyze the influence of grid resolution on the results, and an uncertainty analysis to assess the impact of various assumptions and parameters on the outcomes. After confirming the validity of the model, we will present the hydrodynamic results, which describe the flow characteristics and key performance parameters for the system under study. These findings will lay the foundation for the subsequent hydroacoustic analysis.

4.1 Hydrodynamic Results

This section provides an overview of the hydrodynamic results derived from the simulations. Before delving into the detailed results, it is essential to first ensure the accuracy and reliability of the computational model through validation and verification procedures. These steps are critical for confirming that the numerical simulations reflect real-world conditions accurately. Following this, we will present the hydrodynamic results, which offer insights into the flow dynamics, performance, and behavior of the system being analyzed.

4.1.1 Validation And Verification

A validation study was carried out to assess the numerical result uncertainties using the Grid Convergence Index (GCI) approach, which relies on the Richardson extrapolation technique [36]. This approach was initially proposed by Roache [37] and has been extensively applied in the literature, following the procedure outlined by Celik et al. [38].

The variables N_1, N_2 and N_3 denote the total number of grids employed in the numerical computations, whereas h_1, h_2 and h_3 represent the corresponding grid

sizes. The volume of the i'th grid is represented by ΔV_i , and the refinement ratios r_{21} and r_{32} are expressed as follows:

$$r_{21} = \frac{h_2}{h_1} \tag{4.1}$$

$$r_{32} = \frac{h_3}{h_2} \tag{4.2}$$

It is important to recognize that, as stated by Celik et al. [38], a refinement ratio greater than 1.3 is advisable. In this study, a refinement ratio of was adopted, which is typically employed in CFD applications. The difference between the solution scalars (ε) can be determined using the following equation:

$$\begin{aligned} \varepsilon_{21} &= \varphi_2 - \varphi_1, \\ \varepsilon_{32} &= \varphi_3 - \varphi_2 \end{aligned} \tag{4.3}$$

Here, φ_1, φ_2 and φ_3 represent the numerical results obtained from the coarse, medium, and fine grids, respectively. The solution scalar is defined as the dimensionless total resistance of the submarine model at a service speed of F_r = 0.4667.

The convergence condition (R) of the numerical analysis and the apparent order (p) can be evaluated using equation (4.4) and (4.6), respectively.

$$R = \frac{\varepsilon_{21}}{\varepsilon_{32}} \tag{4.4}$$

Equation below explains the ratio R's mathematical meaning.

- $-1 < R < 0$ Oscillatory convergence
- $0 < R < 1$ Monotonic convergence
- $R < -1$ Oscillatory divergence
- $1 < R$ Monotonic divergence

The extrapolated value can be calculated using the following equation:

$$\varphi_{ext}^{21} = \left(\frac{r^p \varphi_1 - \varphi_2}{r^p - 1}\right) \tag{4.5}$$

Here, p is the apparent order of the method, determined using the following equation:

$$p = \frac{\left| ln \left| \frac{\varepsilon_{32}}{\varepsilon_{21}} \right| + q(p) \right|}{\ln(r_{21})} \tag{4.6}$$

Here, q(p) and s can be defined as follows:

$$q(p) = \ln\left(\frac{r_{21}^p - s}{r_{32}^p - s}\right) \tag{4.7}$$

$$\mathrm{s} = \mathrm{sgn}\left(\frac{\varepsilon_{32}}{\varepsilon_{21}}\right) \tag{4.8}$$

The approximate relative error (e_a^{21}) and the extrapolated relative error (e_{ext}^{21}) are defined as follows:

$$e_a^{21} = \left| \frac{\varphi_1 - \varphi_2}{\varphi_1} \right|, e_{ext}^{21} = \left| \frac{e_{ext}^{12} - \varphi_1}{e_{ext}^{12}} \right| \tag{4.9}$$

The GCI can be determined using the following formula:

$$GCI_{Fine}^{21} = \frac{1.25 * e_a^{21}}{r_{21}^p - 1} \tag{4.10}$$

Table 4.1 provides the uncertainty levels estimated for the DARPA Suboff submarine model employed in the numerical simulations.

Table 4.1 Results of uncertainity analysis in terms of submarine total resistance

Grid Convergence			
φ_1	102.809	R	0.5964
φ_2	102.317	Φ_{ext}^{21}	103.5359
φ_3	101.492	e_a^{21}	0.0048
ε_{21}	-0.492	e_{ext}^{21}	0.0070
ε_{32}	-0.825	GCI_{Fine}^{21}	0.0088

As presented in Table 4.1 the R value satisfies the second condition outlined earlier and exhibits monotonic convergence. Additionally, the uncertainty is estimated to be around 0.89%. Alongside the uncertainty analysis, a mesh dependency study was conducted to validate the simulation results against the experimental total resistance value of 102.3 N. The findings of this study are presented in Table 4.2, highlighting the relationship between mesh resolution and the accuracy of the predicted force values.

Table 4.2 Results of mesh dependency

	Cell number	Total Force [N]	Relative Difference (%) (Comparision with experimental results)
Coarse	861925	102.809	0.5
Medium	1734514	102.317	0.02
Fine	3480180	101.492	0.79

4.1.2 Results of Hydrodynamic Analysis

The accuracy of the computational fluid dynamics (CFD) calculations employed in evaluating ship resistance has been assessed through simulations of the DARPA AFF-8 submarine form. These analyses were conducted to validate the numerical approach utilized in this study.

Figure 4.1 illustrates a comparison between the numerical results for the DARPA Suboff AFF-8 obtained in this research and the numerical data from Dogrul [39], as well as the experimental data from Liu and Huang [40]. The findings indicate that the numerical results for all forward speeds closely align with the experimental data, demonstrating an excellent correlation.

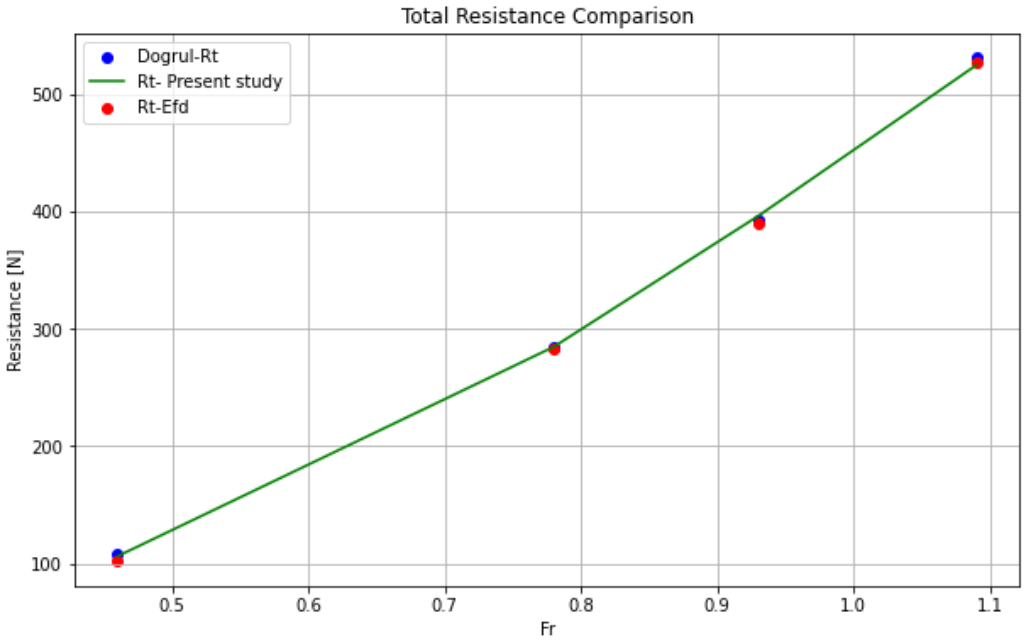

Figure 4.1 Computational comparison of total resistance for submarine

Figure 4.2 illustrates the free surface elevation at L/8. When the submarine operates near the free- surface, it produces a wave field on the still water. A wave crest forms close to the bow, while the wave trough is positioned toward the aft section of the hull. This wave formation leads to additional wave drag acting on the submarine. As expected, the total resistance increases in near-surface conditions due to wave drag, which is not present during deep-water operations.

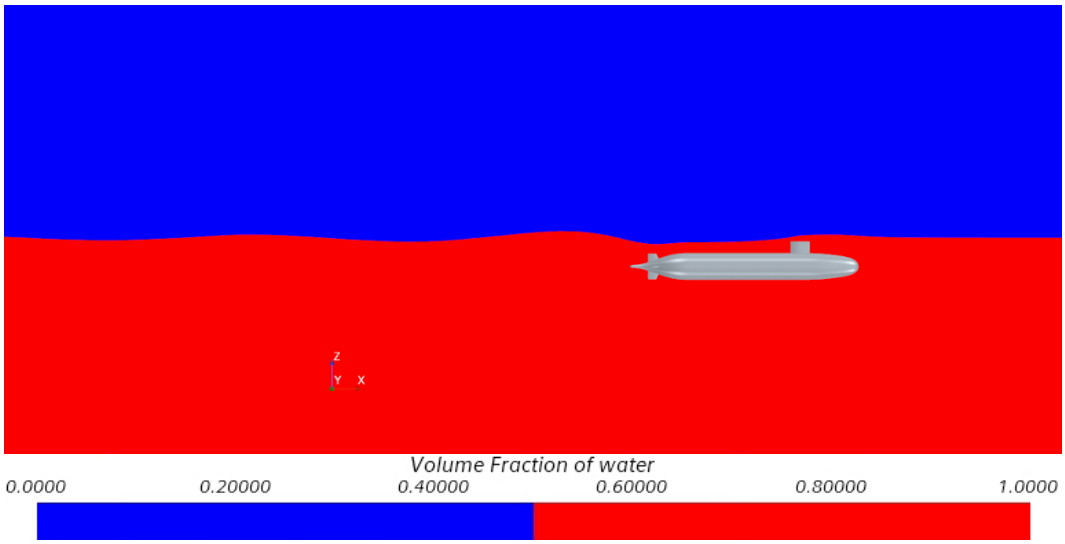

Figure 4.2 The elevation of the free surface from side view for the L/8 depth and F_r=0.466 condition

As the submarine moves away from the free water surface, it begins to behave as if it is fully submerged, with negligible effects from the free surface. However, as it approaches the free surface, noticeable deformations of the free surface become evident, accompanied by an increase in total resistance, as also demonstrated in Figure 4.3, where it can be observed that total resistance decreases as the submarine moves further away from the free surface.

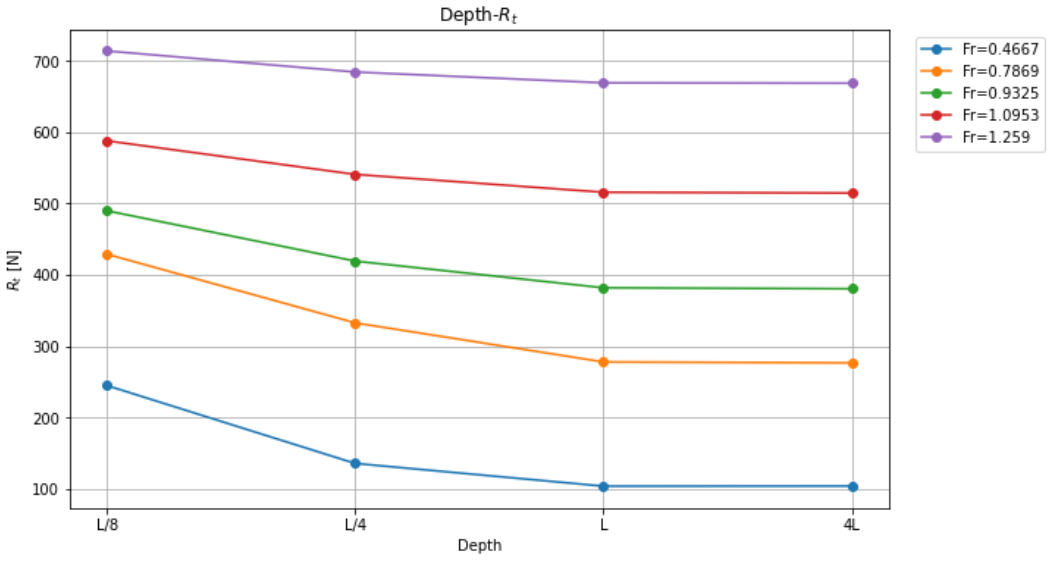

Figure 4.3 Total resistance results for all analyeses

Figure 4.4 provides an overview of the free surface deformations around the submarine. The wave elevation near the bow generates a diverging wave pattern. Although the submarine does not pierce the surface, the resulting wave field resembles the characteristics of Kelvin waves.

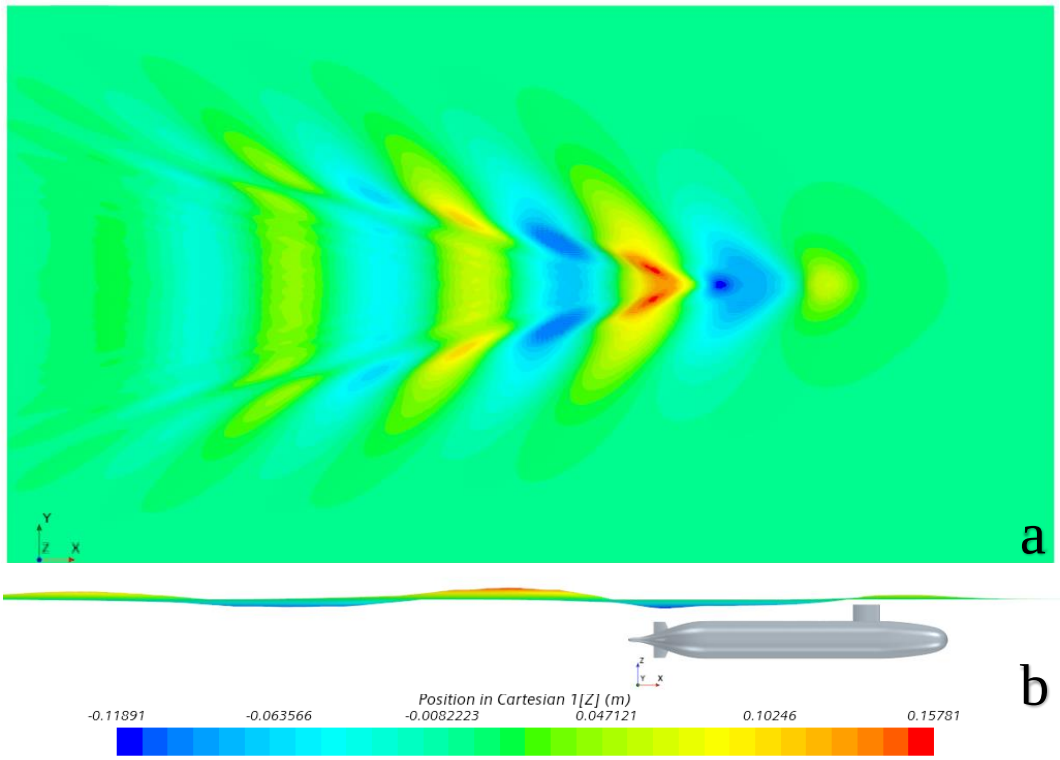

Figure 4.4 The wave field around hull; a is top view, b is side view for the L/8 depth and Fr=0.466 condition

Figure 4.5 presents the velocity field around the submarine under both deep-water and near-surface conditions. When the submarine operates close to the water surface, the flow around the bow interacts with the free surface, with similar interactions observed near the aft section. Additionally, the velocity field in the wake at L/8 shows significant asymmetry compared to the symmetrical flow observed in deep-water conditions (no free surface effect).

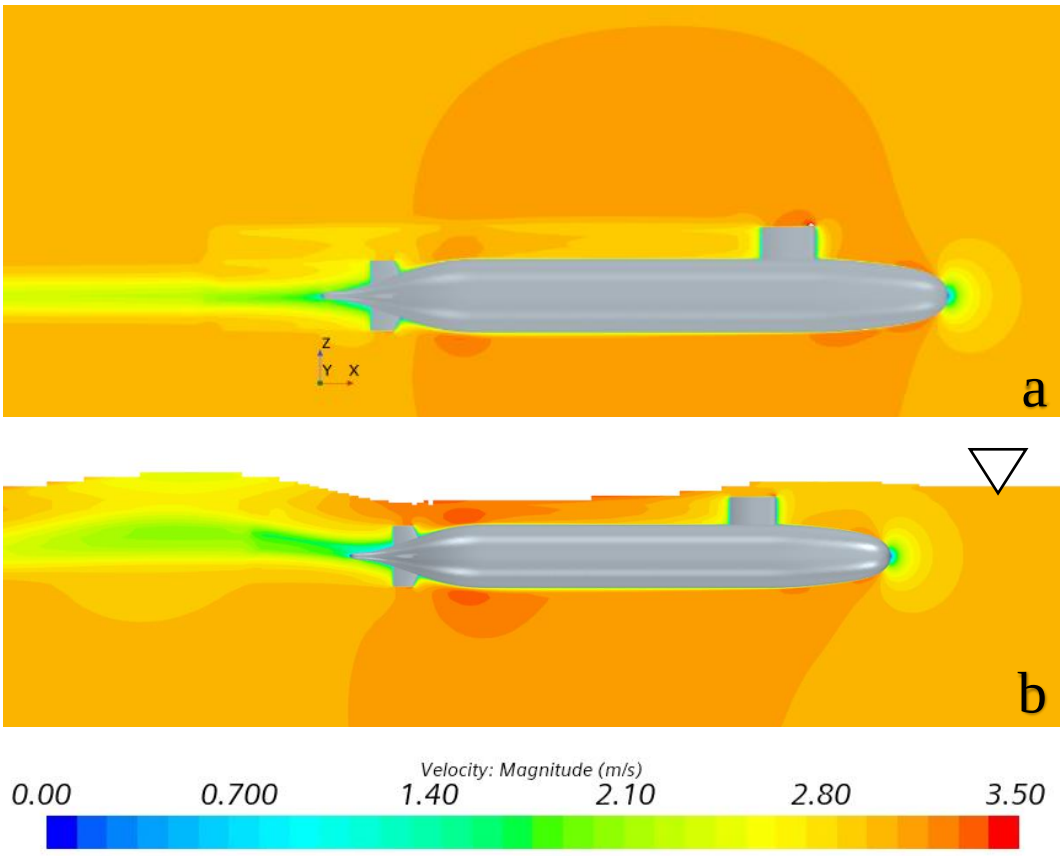

Figure 4.5 Velocity field around submarine, a is for deep water condition, b is for L/8 depth and Fr=0.466 condition

4.2 Hydroacoustic Results

This section focuses on the hydroacoustic results obtained from the simulations, highlighting the noise characteristics and sound pressure levels generated by the flow around the geometry. The analysis builds upon the validated hydrodynamic results to investigate the acoustic behavior in the underwater environment. Key metrics, such as frequency spectra and spatial distribution of sound pressure levels, will be presented to provide a comprehensive understanding of the noise generation mechanisms. These findings are crucial for evaluating the acoustic performance and identifying potential noise mitigation strategies.

Regions with high vorticity in turbulent flows are often associated with increased noise levels due to larger velocity and pressure gradients. These steep gradients cause rapid fluctuations in the flow field, which generate forces on nearby surfaces, leading to sound propagation. The interaction of turbulent eddies and these gradients is a key factor in noise generation. The vorticity distribution of the flow at L/8 depth for Fr=1.259 is presented in Figure 4.6.

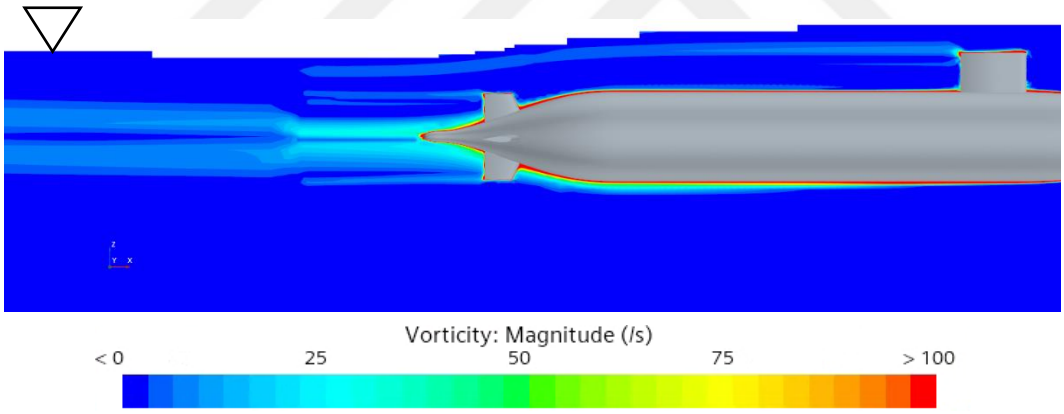

Figure 4.6 Vorticity distribution of flow for L/8 depth and Fr=1.259 condition

Figure 4.7 illustrates the flow field around a submarine, visualized using the Q-Criterion method to identify vortical structures. The Q-Criterion, defined as the second invariant of the velocity gradient tensor, is a widely used method to distinguish vortices in turbulent flows. This representation provides insight into the vortex dynamics and flow separations caused by the submarine's geometry.

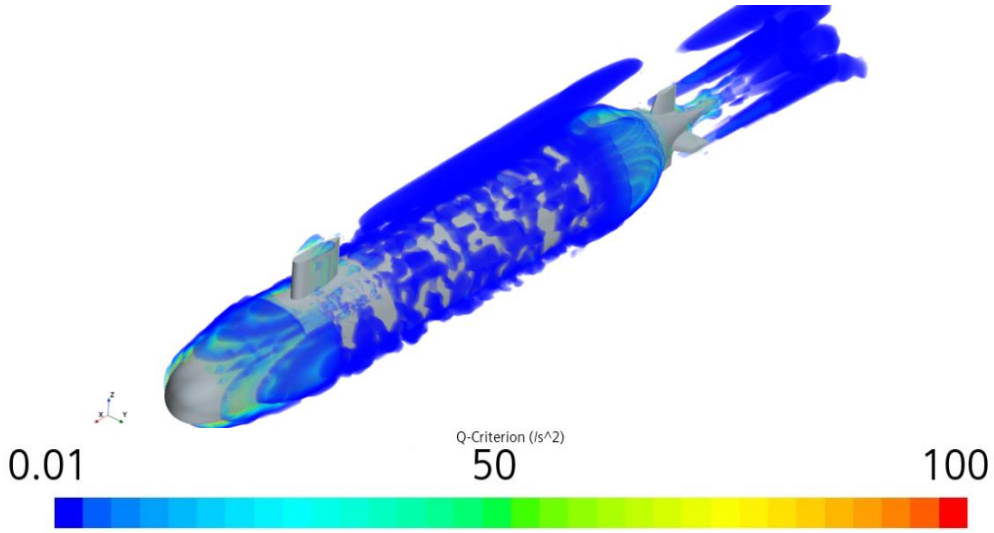

Figure 4.7 Flow field around a submarine for L/8 depth and Fr=1.259 condition

In the forebody region, small-scale vortices form due to flow separation near the bow, indicated by low Q-Criterion values represented in blue. Moving downstream, significant vortex structures develop around the sail. These sail-induced vortices, visible in green and yellow, are the result of shear layers and flow separation interacting with the sail geometry, contributing to drag and potential acoustic noise.

In the stern region, intense vortex activity is observed, particularly near the aft. The tip vortices originating from the rudder are clearly visible. These regions represent strong vorticity and play a significant role in wake dynamics and noise generation. Further downstream, the wake region exhibits a complex interaction of vortices, where structures from the sail and stern merge and dissipate.

This visualization provides valuable insights into the flow behavior, emphasizing regions critical for optimizing the submarine's performance and minimizing its acoustic signature. By analyzing the wake dynamics and the interplay of vortices, researchers can better understand the aerodynamic and noise-related challenges associated with such complex geometries.

In Figure 4.7, it is observed that the turbulence viscosity behind the submarine decreases as the position shifts from deeper regions toward the free water surface. In deeper regions, an increase in turbulence kinetic energy (k) leads to an increase in turbulence viscosity (μ_t). However, as the flow approaches the free surface, changes in boundary conditions and the effects of the free surface cause a reduction in turbulence kinetic energy.

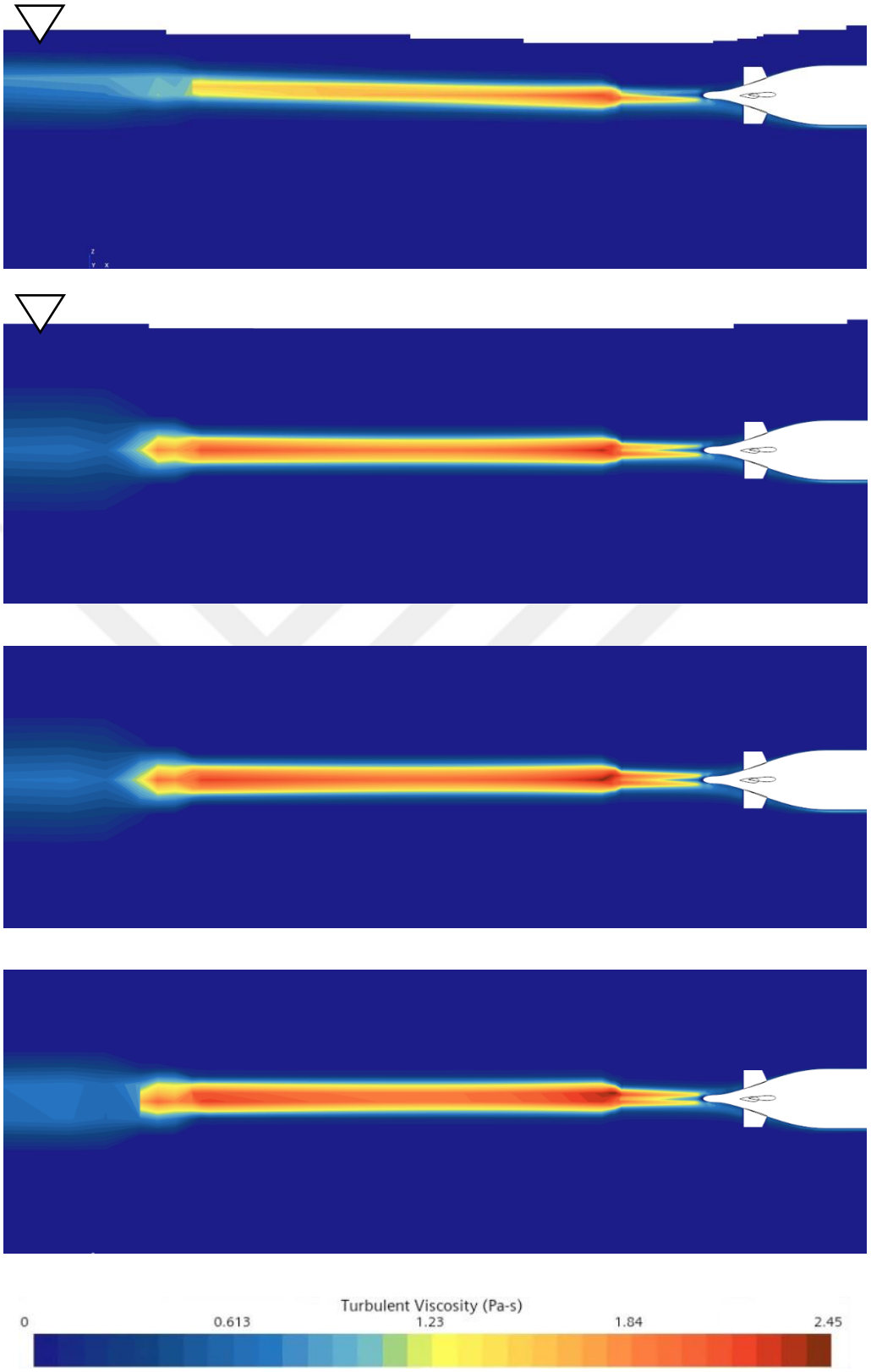

Figure 4.8 Flow field around a submarine for L/8, L/4, L, 4L depth respectively and Fr=1.259 condition

In Figure 4.9 illustrates the variation in flow streamlines and vorticity magnitude in the wake region of the submarine at different depths. As the submarine approaches the free water surface, an increase in vorticity magnitude is observed, with the streamlines orienting and accelerating towards the surface. At greater depths, the vorticity magnitude decreases, and the streamlines exhibit a more uniform distribution. These findings highlight the significant influence of the free water surface on the hydrodynamic structures around the submarine.

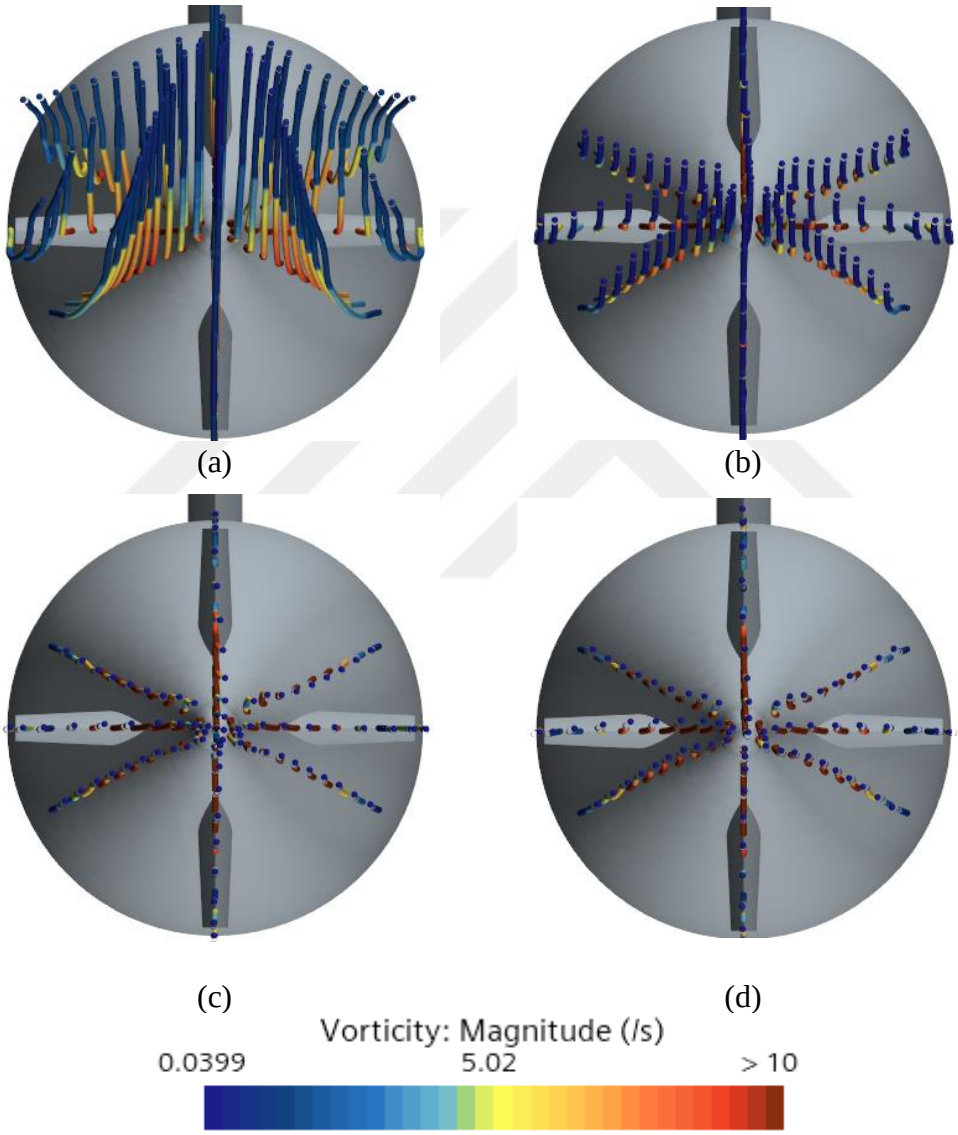

Figure 4.9 Vorticity lines around wake region for L/8, L/4, L, 4L depth respectively and Fr=1.259 condition

As observed in Figure 4.10, as the submarine approaches the free surface, the flow accelerates, and the pressure in the region decreases. This results in the formation of a reverse vacuum effect in areas near the free surface. The acceleration of the flow is associated with an increase in the kinetic energy of the fluid, which leads to

a reduction in pressure. This phenomenon causes dynamic pressure drops in regions where the flow velocity increases, particularly near the water surface.

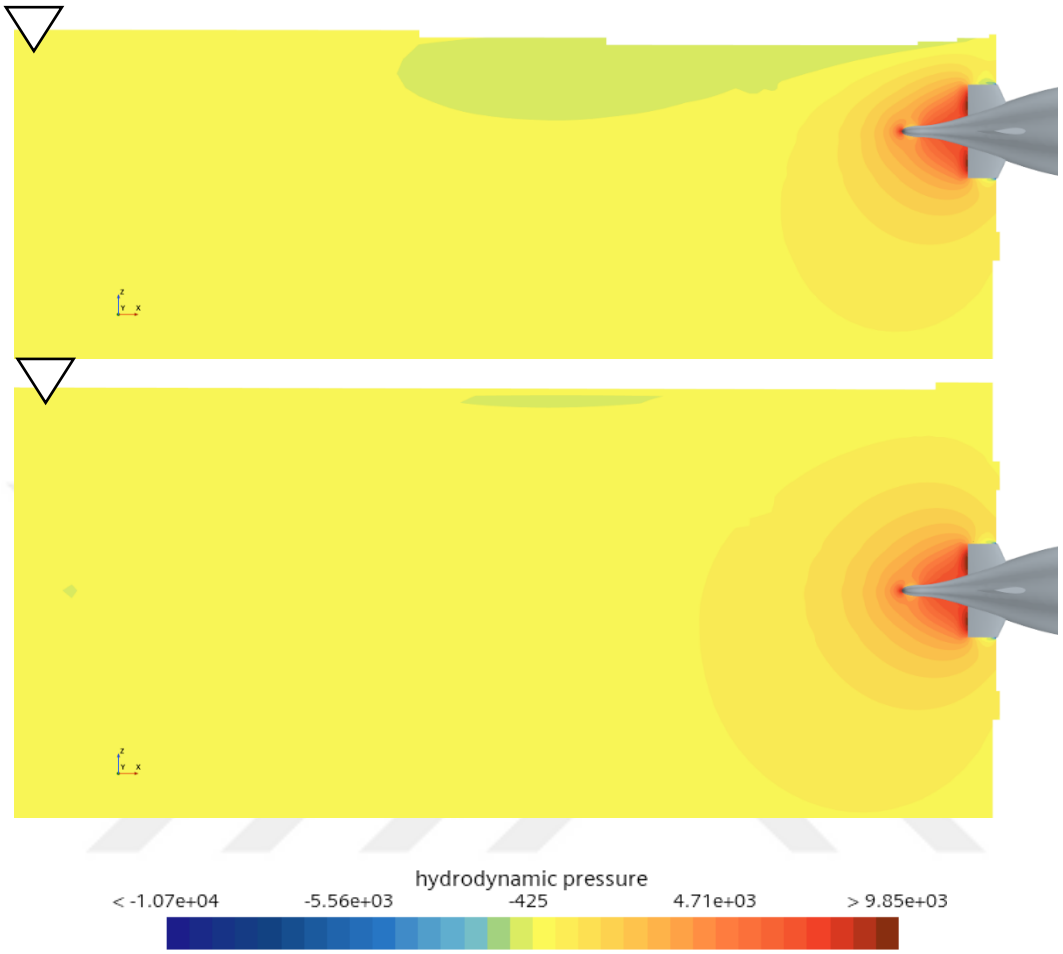

Figure 4.10 Hydrodynamic pressure for L/8, L/4 depth respectively and Fr=1.259 condition

The volumes of the vortices were thoroughly analyzed, Figure 4.11, revealing that their size diminishes as they extend further away from the free water surface and into deeper regions. This observation highlights the influence of depth on vortex dynamics, where proximity to the surface facilitates larger vortex structures due to higher energy availability and interaction with surface flows. Moreover, it was noted that an increase in flow velocity directly correlates with a rise in turbulence intensity. This is attributed to the fact that a higher Reynolds number, which is a function of velocity, indicates a more turbulent flow regime. As the Reynolds number grows, the chaotic behavior within the flow intensifies, leading to greater energy dissipation and more pronounced turbulence. These findings are critical for understanding flow behavior in marine and hydrodynamic applications, as they

provide insights into the interaction between depth, velocity, and turbulence, which are essential for designing efficient and noise-minimizing underwater structures.

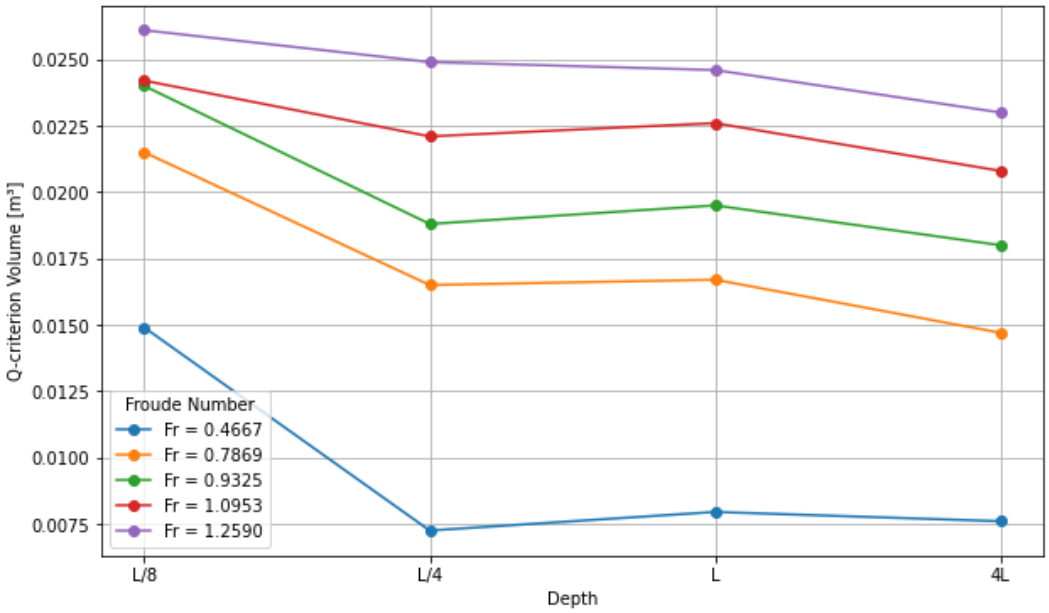

Figure 4.11 The volumes of the vortices depending on depth

Figure 4.12 illustrates that as the distance from the source increases, the dominant frequency remains constant, but the sound pressure level decreases. The obtained RMS values show that the sound pressure levels are higher for receivers closer to the source, and decrease as the distance from the source increases. This indicates that sound energy diminishes with distance, and environmental factors also play a role in this reduction. Receivers closer to the source experience higher sound pressure levels, while those farther away exhibit lower RMS values. This result highlights the attenuation of sound with increasing distance and contributes to a better understanding of the relationship between frequency and sound pressure.

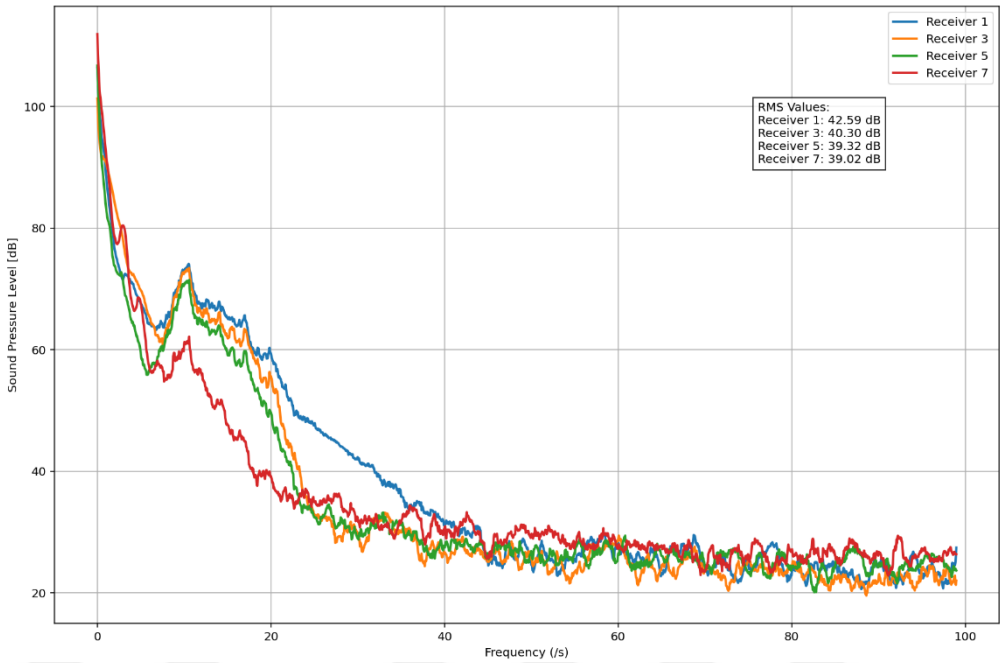

Figure 4.12 Relationship between frequency and sound pressure level for receiver 1, 3, 5, and 7 for depth L/4 and Fr=1.0953.

The obtained results were evaluated based on velocity and depth

4.2.1 Effect on Depth on Hydrodynamic Noise

Hydrodynamic noise, which is primarily caused by the motion of water and the behavior of vortices within it, is an important consideration in various marine applications. One of the key factors influencing hydrodynamic noise is the depth at which the phenomenon occurs. As depth increases, several changes in the flow dynamics take place, including alterations in vortex formation, turbulence intensity, and flow stability, all of which contribute to variations in noise levels. Near the free water surface, the flow is typically more unstable and turbulent, leading to higher noise intensities. In deeper regions, the flow tends to stabilize, and vortex sizes generally decrease, which can reduce the overall noise produced. Understanding the impact of depth on hydrodynamic noise is essential for assessing acoustic emissions in marine environments and for the design of quieter underwater vehicles and structures. This section explores the relationship between water depth and noise generation, focusing on how depth influences the characteristics of vortices and turbulence, which are the primary sources of hydrodynamic noise.

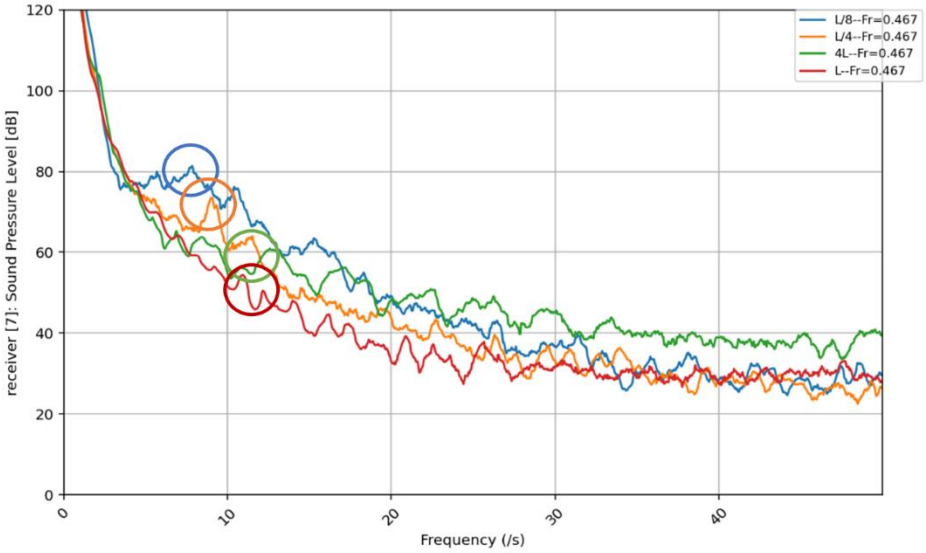
L/8--Fr=0.467
L/4--Fr=0.467
4L--Fr=0.467
L--Fr=0.467
receiver [7]: Sound Pressure Level [dB]
Frequency (/s)

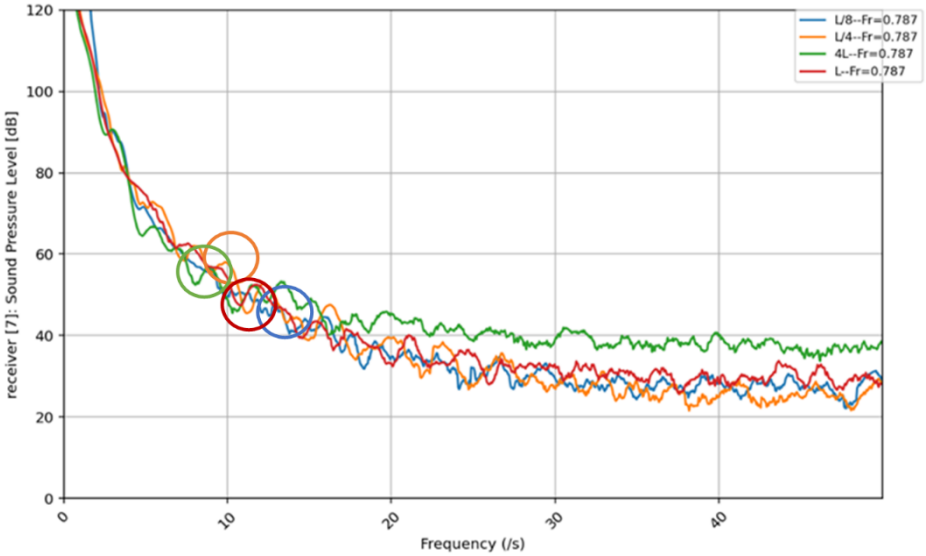
L/8--Fr=0.787
L/4--Fr=0.787
4L--Fr=0.787
L--Fr=0.787
receiver [7]: Sound Pressure Level [dB]
Frequency (/s)

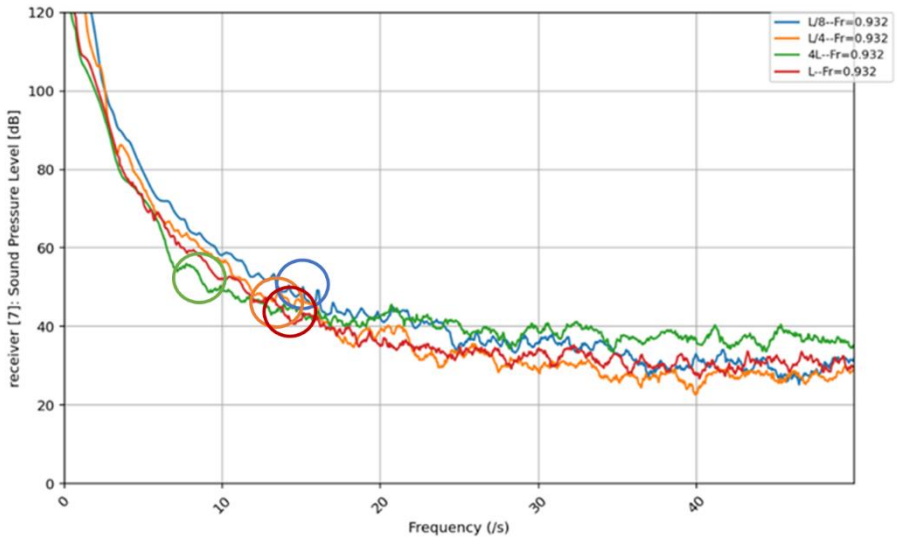
L/8--Fr=0.932
L/4--Fr=0.932
4L--Fr=0.932
L--Fr=0.932
receiver [7]: Sound Pressure Level [dB]
Frequency (/s)

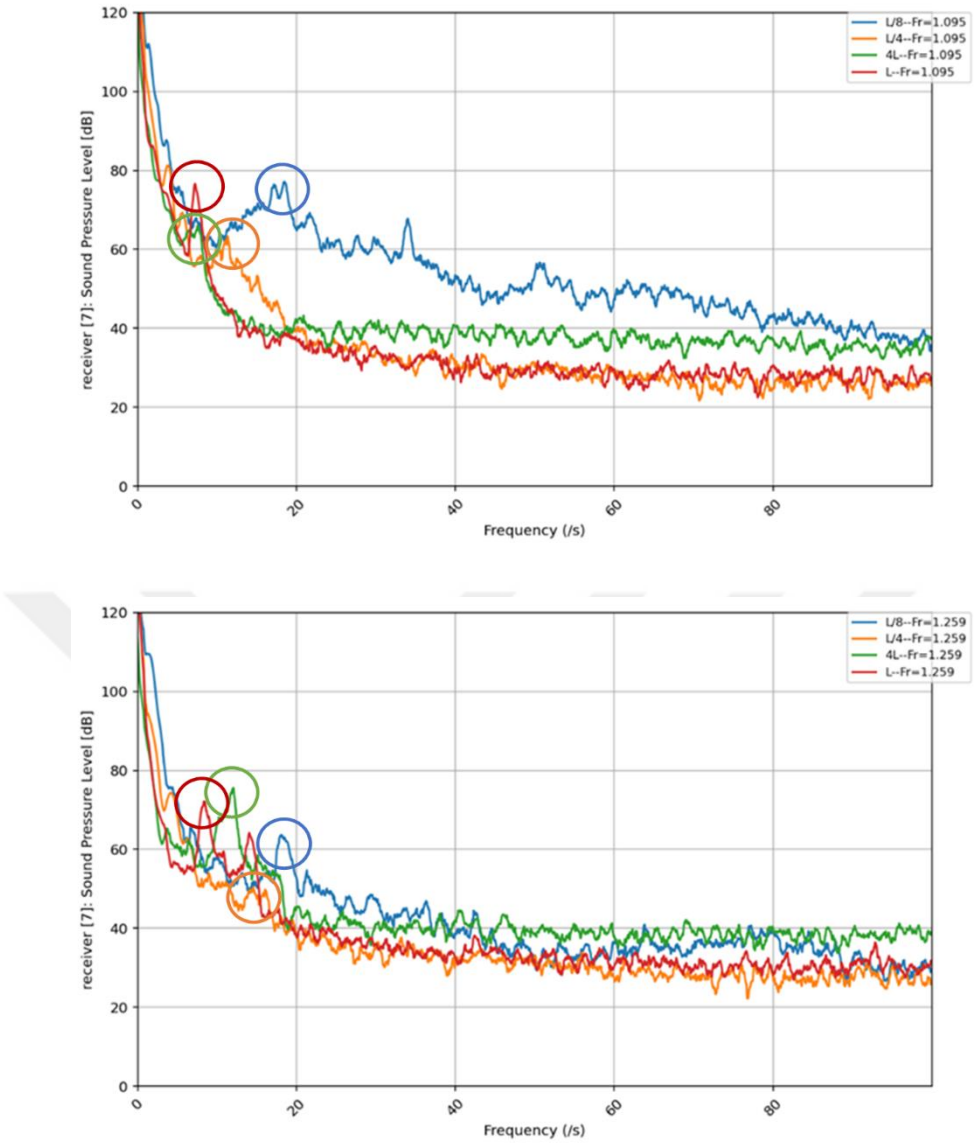

Figure 4.13 Sound pressure level results in the frequency domain at receiver 7. froude numbers are Fr = 0.4667, 0.7869, 0.9325, 1.0953, and Fr=1.259, respectively.

The excessive fluctuations in the obtained data reduce their interpretability. To enhance clarity and facilitate better understanding, a smoothing process was applied using the moving average method. This approach preserves the underlying trends in the data while minimizing short-term variations, thereby providing a clearer representation of the overall behavior.

Table 4.3 Dominant frequency results for the Effect of Distance from Free Water Surface

		Dominant Frequency (Hz)	**SPL (dB)**
Fr = 0.467	L/8	8	80
	L/4	9	76
	L	9	55
	4L	11	60
Fr = 0.787	L/8	12	50
	L/4	10	58
	L	11	56
	4L	12	57
Fr = 0.932	L/8	16	43
	L/4	15	38
	L	12	41
	4L	13	41
Fr = 1.0995	L/8	18	77
	L/4	15	62
	L	10	76
	4L	11	63
Fr = 1.259	L/8	19	62
	L/4	18	49
	L	10	75
	4L	12	76

4.2.2 Effect on Velocity on Hydrodynamic Noise

Velocity is a critical factor influencing hydrodynamic noise, as it directly affects the flow characteristics and turbulence levels within the fluid. As the flow velocity increases, the Reynolds number rises, signifying a transition to more turbulent and chaotic flow regimes. This heightened turbulence intensifies noise generation by amplifying pressure fluctuations and vortex shedding frequencies, which are key contributors to hydrodynamic noise. Faster flow also results in more significant energy dissipation, leading to higher acoustic emissions. Understanding the relationship between velocity and hydrodynamic noise is essential for predicting and managing noise levels in marine environments, such as those around ships, underwater vehicles, and other submerged structures. This section examines how changes in velocity influence turbulence, vortex behavior, and noise generation, providing insights for optimizing designs to minimize noise while maintaining efficient flow dynamics.

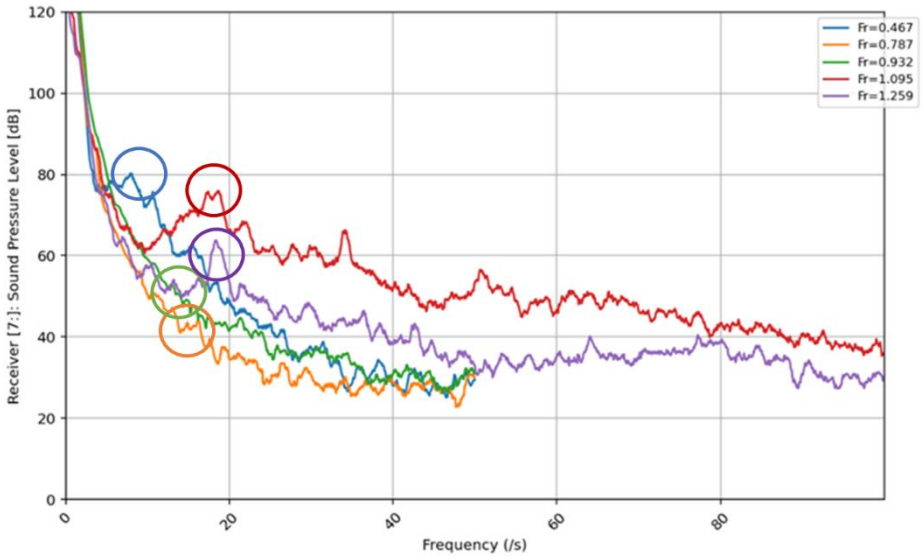

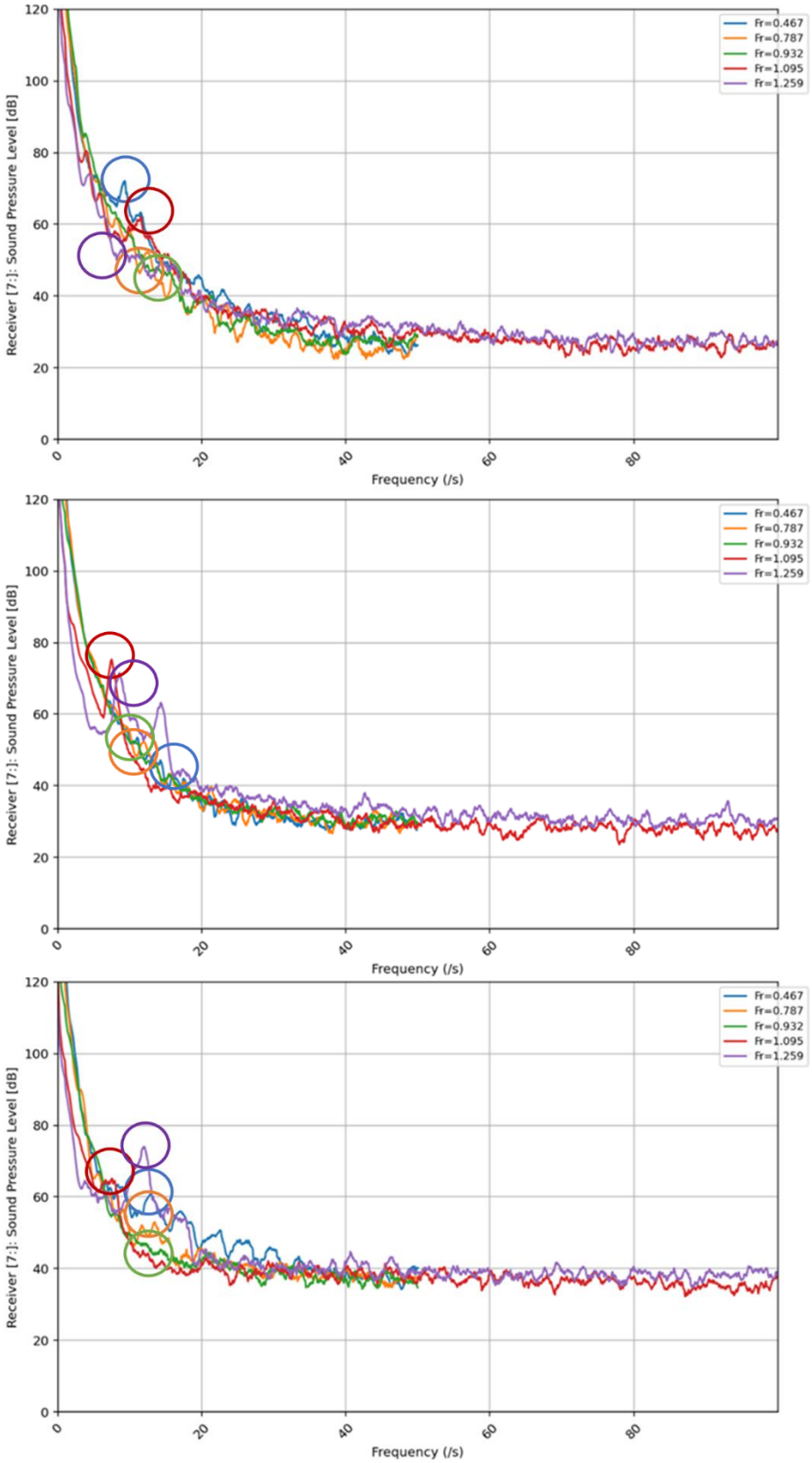

Figure 4.14 Sound Pressure Level (SPL) results in the frequency domain at receiver 7. Depths are L/8, L/4, L. 4L respectively

In the analysis, it was observed that as flow velocity increases, the SPL values rise correspondingly. This relationship can be attributed to the intensification of turbulent structures and vorticity at higher velocities, which act as dominant noise sources. The increased velocity amplifies the pressure and velocity gradients within the flow field, leading to greater acoustic emissions. This trend highlights the direct correlation between flow speed and noise generation.

When the submarine operates near the free surface, the dominant frequency amplitude shows increase under conditions of higher velocity. This behavior can be attributed to the interaction between the free surface and the flow dynamics around the submarine, which intensifies the generation of acoustic energy at specific frequencies. The proximity to the free surface amplifies these effects due to the increased flow disturbances and interactions with the surface.

In contrast, at the same velocity, as the submarine moves further away from the free surface, the dominant frequency magnitude begins to decrease. This reduction is likely due to the diminished influence of free surface effects on the flow dynamics, resulting in a more stabilized flow field. With reduced surface interactions, the generation of acoustic energy at dominant frequencies becomes less pronounced. These observations underscore the critical role of the free surface in influencing acoustic characteristics, particularly in altering the amplitude of dominant frequencies based on the submarine's depth and operational velocity.

Table 4.4 Dominant frequency results in terms of the effect of the influence of flow velocity

	F_r	Dominant Frequency (Hz)	SPL (dB)
L/8	0.47	8	80
	0.79	12	50
	0.93	16	43
	1.1	18	77
	1.26	19	62

Table 4.4 Dominant frequency results in terms of the effect of the influence of flow velocity (continued…)

	F_r	Dominant Frequency (Hz)	SPL (dB)
L/4	0.47	9	76
	0.79	10	58
	0.93	15	42
	1.1	15	62
	1.26	18	49
L	0.47	9	55
	0.79	11	56
	0.93	12	41
	1.1	10	76
	1.26	10	75
4L	0.47	11	60
	0.79	12	57
	0.93	13	41
	1.1	11	63
	1.26	12	76

5
CONCLUSION

This thesis focuses on the determination of flow-induced noise around a generic submarine using computational fluid dynamics (CFD) methods. Addressing a significant gap in the literature, the study investigates the impact of key parameters, such as velocity and depth, on flow-induced noise. Unlike the majority of existing research that primarily considers propeller noise, the dominant source of underwater acoustic, this work emphasizes noise generated by the flow itself, offering a more detailed exploration of this less-studied aspect of underwater acoustics.

The study was carried out using the DARPA AFF-8 submarine, a well-established generic model with extensively documented hydrodynamic characteristics. Initially, the flow around the submarine was resolved using CFD techniques, and the results were validated against experimental data to ensure accuracy. This validation was critical for establishing the reliability of the hydrodynamic simulations. Subsequently, the Ffowcs Williams-Hawkings (FW-H) acoustic method was employed to assess the submarine's acoustic characteristics under varying velocity and depth conditions.

The findings reveal that both depth and velocity significantly influence the generation of flow-induced noise. High-vorticity regions, particularly in the stern and wake areas, were identified as critical sources of acoustic noise due to rapid velocity and pressure fluctuations. Depth-dependent vortex behavior showed that as depth increases, vortex volumes decrease, resulting in reduced noise levels due to the stabilization of the flow. Conversely, higher flow velocities were associated with increased turbulence intensity, as indicated by rising Reynolds numbers, leading to enhanced noise emissions. The Q-Criterion method effectively

visualized vortical structures, highlighting the significance of geometric features like the sail and rudder in influencing wake dynamics and noise propagation.

Environmental factors, such as proximity to the free water surface, further complicate the flow dynamics. As the submarine approaches the surface, acceleration in flow velocity and reductions in turbulence viscosity emphasize the influence of boundary conditions. These findings provide critical insights into the hydrodynamic structures around the submarine and their contribution to noise generation. Additionally, the attenuation of sound pressure levels with distance from the source highlights the interplay between sound energy dissipation and environmental influences.

When the submarine operates near the free surface, the dominant frequency amplitude increases at higher velocities due to intensified flow disturbances and interactions with the surface. However, as the submarine moves further away from the free surface at the same velocity, the dominant frequency magnitude decreases, as the flow becomes more stabilized and surface effects diminish. This highlights the significant influence of the free surface on acoustic characteristics, particularly in altering dominant frequencies based on depth and velocity.

The contributions of this study extend beyond the specific case of the DARPA AFF-8 submarine. The methodology and findings have broader implications for understanding the dynamics of flow-induced noise in submerged environments, particularly for marine applications where minimizing acoustic signatures is critical, such as in naval operations and environmental monitoring. By combining detailed hydrodynamic and acoustic analyses, this research lays the groundwork for designing quieter submarine structures and improving underwater noise predictions in diverse operational scenarios.

Future work should focus on integrating the effects of propeller noise into the analysis. Propellers, as dominant noise sources, interact with flow dynamics to create complex acoustic patterns. Incorporating propeller noise models and comparing them with the flow-induced noise characterized in this study would enable a more precise evaluation of hydrodynamic noise and its role in overall acoustic emissions. Additionally, exploring other parameters, such as surface roughness, hull geometry, and varying environmental conditions, could provide

further insights into noise reduction strategies and support the development of advanced acoustic prediction tools for marine vehicles.

In conclusion, this study provides comprehensive insights into the interplay between flow dynamics and acoustic emissions, emphasizing the importance of addressing multiple noise sources. The results contribute to a deeper understanding of flow-induced noise mechanisms, supporting the design of quieter and more efficient underwater vehicles.

REFERENCES

[1] D. Ross, “Mechanics of underwater noise.” Accessed: Oct. 06, 2023. [Online]. Available: https://apps.dtic.mil/sti/citations/ADA075101

[2] The Specialist Committee on Hydrodynamic Noise, “The specialist committee on hydrodynamic noise final report and recommendations to the 28th ITTC,” https://www.ittc.info/media/7837/17-sc-hydrodynamic-noise-compressed.pdf.

[3] M. J. Lighthill and M. H. A. Newman, “On sound generated aerodynamically I. general theory,” *Proc R Soc Lond A Math Phys Sci*, vol. 211, no. 1107, pp. 564–587, Jan. 1997, doi: 10.1098/rspa.1952.0060.

[4] M. J. Lighthill, “On sound generated aerodynamically II. turbulence as a source of sound,” *Proc R Soc Lond A Math Phys Sci*, vol. 222, no. 1148, pp. 1–32, Jan. 1997, doi: 10.1098/rspa.1954.0049.

[5] J. E. Ffowcs Williams, D. L. Hawkings, and M. J. Lighthill, “Sound generation by turbulence and surfaces in arbitrary motion,” *Philosophical Transactions of the Royal Society of London. Series A, Mathematical and Physical Sciences*, vol. 264, no. 1151, pp. 321–342, Jan. 1997, doi: 10.1098/rsta.1969.0031.

[6] F. Farassat and L. R. Center., *Theory of noise generation from moving bodies with an application to helicopter rotors*. in NASA technical report ;NASA TR R-451. Washington, D.C. : [Springfield, Va.: National Aeronautics and Space Administration ; For sale by the National Technical Information Service], 1975. [Online]. Available: https://catalog.hathitrust.org/Record/100075891

[7] F. Farassat and G. P. Succi, “A review of propeller discrete frequency noise prediction technology with emphasis on two current methods for time

domain calculations," *J Sound Vib*, vol. 71, no. 3, pp. 399–419, 1980, doi: https://doi.org/10.1016/0022-460X(80)90422-8.

[8] F. Farassat, "Derivation of formulations 1 and 1A of Farassat," VA, United States, Mar. 2007. [Online]. Available: https://ntrs.nasa.gov/citations/20070010579

[9] F. Farassat, "Linear acoustic formulas for calculation of rotating blade noise," *AIAA Journal*, vol. 19, no. 9, pp. 1122–1130, Sep. 1981, doi: 10.2514/3.60051.

[10] K. Wang, T. Zhang, Y. O. Zhang, J. M. Liu, and C. Z. Wang, "Numerical simulations of hydrodynamic noise of an underwater vehicle," in *OCEANS 2014 - TAIPEI*, 2014, pp. 1–9. doi: 10.1109/OCEANS-TAIPEI.2014.6964348.

[11] S. Yao, P. Guang, and H. Q. Gao, "LES-based numerical simulation of flow noise for UUV with full appendages," *Adv Mat Res*, vol. 631–632, pp. 879–884, 2013, doi: 10.4028/www.scientific.net/AMR.631-632.879.

[12] C. Yu, R. Wang, X. Zhang, and Y. Li, "Experimental and numerical study on underwater radiated noise of AUV," *Ocean Engineering*, vol. 201, p. 107111, 2020, doi: https://doi.org/10.1016/j.oceaneng.2020.107111.

[13] M. Wang, J. B. Freund, and S. K. Lele, "Computational prediction of flow-generated sound," *Annu Rev Fluid Mech*, vol. 38, no. 1, pp. 483–512, Dec. 2005, doi: 10.1146/annurev.fluid.38.050304.092036.

[14] H. Zhang and K. Duan, "Flow noise computation and tail wing optimization of the underwater vehicle based on computational fluid dynamics," *Journal of Vibroengineering*, vol. 17, no. 5, pp. 2633–2644, 2015.

[15] Y. Liu, Y. Li, and D. Shang, "The generation mechanism of the flow-ınduced noise from a sail hull on the scaled submarine model," *Applied Sciences 2019, Vol. 9, Page 106*, vol. 9, no. 1, p. 106, Dec. 2018, doi: 10.3390/APP9010106.

[16] S.-J. Yeo, S.-Y. Hong, J.-H. Song, H.-W. Kwon, and H.-S. Seol, "Integrated analysis of flow-induced noise from submarine under snorkel condition," *Proceedings of the Institution of Mechanical Engineers, Part M: Journal of*

Engineering for the Maritime Environment, vol. 234, no. 4, pp. 771–784, Jun. 2020, doi: 10.1177/1475090220916594.

[17] M. Bagheri, H. Mehdigholi, M. Seif, and O. Yaakob, "An experimental and numerical prediction of marine propeller noise under cavitating and non-cavitating conditions," *Brodogradnja*, vol. 66, pp. 29–45, Jun. 2015.

[18] A. Rocca, M. Cianferra, R. Broglia, and V. Armenio, "Computational hydroacoustic analysis of the BB2 submarine using the advective ffowcs williams and hawkings equation with wall-modeled LES," *Applied Ocean Research*, vol. 129, Dec. 2022, doi: 10.1016/J.APOR.2022.103360.

[19] C. X. Wang, L. Huang, Y. Zhao, J. C. Dai, and Y. C. Jiang, "Influence of stern rudder type on flow noise of underwater vehicles," *J Mar Sci Eng*, vol. 10, no. 12, 2022, doi: 10.3390/jmse10121866.

[20] D. Qu, Z. Zhang, and J. Lou, "Analysis of hydrodynamic noise characteristics of rudder-wing," *Vibroengineering PROCEDIA*, vol. 11, pp. 155–160, Jan. 2017, doi: 10.21595/vp.2017.18478.

[21] P. Kellett, O. Turan, and A. Incecik, "A study of numerical ship underwater noise prediction," *Ocean Engineering*, vol. 66, pp. 113–120, 2013, doi: https://doi.org/10.1016/j.oceaneng.2013.04.006.

[22] J. Abshagen, I. Schäfer, Ch. Will, and G. Pfister, "Coherent flow noise beneath a flat plate in a water tunnel experiment," *J Sound Vib*, vol. 340, pp. 211–220, 2015, doi: https://doi.org/10.1016/j.jsv.2014.11.033.

[23] Z. Ma, P. Li, L. Wang, J. Lu, and Y. Yang, "Mechanistic study of noise source and propagation characteristics of flow noise of a submarine," *Ocean Engineering*, vol. 302, p. 117667, 2024, doi: https://doi.org/10.1016/j.oceaneng.2024.117667.

[24] Ş. Arı, "Yanma odası tasarımının dizel motor gürültüsüne etkilerinin incelenmesi," M.S. thesis, Institute of Science and Technology, Istanbul Technical University, Istanbul, Turkey, 2011. [Online]. Available: https://polen.itu.edu.tr/items/18b1a69f-4dcc-434d-8f63-6cc6428b110b

[25] D. A. Russell, J. P. Titlow, and Y.-J. Bemmen, “Acoustic monopoles, dipoles, and quadrupoles: An experiment revisited,” *Am J Phys*, vol. 67, no. 8, pp. 660–664, Aug. 1999, doi: 10.1119/1.19349.

[26] L. Fenini, S. Malavasi, and R. Barzaghi, “Numerical modelling of flow-induced noise emitted by control devices,” 2023, Accessed: Nov. 15, 2023. [Online]. Available: https://www.politesi.polimi.it/handle/10589/146091

[27] N. Curle and M. J. Lighthill, “The influence of solid boundaries upon aerodynamic sound,” *Proc R Soc Lond A Math Phys Sci*, vol. 231, no. 1187, pp. 505–514, Jan. 1997, doi: 10.1098/rspa.1955.0191.

[28] A. Powell, “Aerodynamic noise and the plane boundary,” *J Acoust Soc Am*, vol. 32, no. 8, pp. 982–990, Aug. 1960, doi: 10.1121/1.1908347.

[29] M. S. Howe, “Contributions to the theory of aerodynamic sound, with application to excess jet noise and the theory of the flute,” *J Fluid Mech*, vol. 71, no. 4, pp. 625–673, Oct. 1975, doi: 10.1017/S0022112075002777.

[30] W. K. Blake, “Chapter 2 - Theory of sound and its generation by flow,” in *Mechanics of Flow-Induced Sound and Vibration, Volume 1 (Second Edition)*, W. K. Blake, Ed., Academic Press, 2017, pp. 47–135. doi: https://doi.org/10.1016/B978-0-12-809273-6.00002-6.

[31] Siemens Digital Industries Software, “Simcenter STAR-CCM+ User guide v. 2021.1,” 2021, pp. 8307–8316.

[32] L. E. Kinsler, A. B. Coppens, A. R. Frey, and J. V. Sanders, *Fundamentals of acoustics*. John Wiley & Sons Inc, 2000.

[33] Siemens Digital Industries Software, “Simcenter STAR-CCM+ User guide v. 2021.1,” 2021, ch. Volume of Fluid Meth, pp. 7872–7908.

[34] T.-H. Shih, W. W. Liou, A. Shabbir, Z. Yang, and J. Zhu, “A new k-ϵ eddy viscosity model for high reynolds number turbulent flows,” *Comput Fluids*, vol. 24, no. 3, pp. 227–238, 1995, doi: https://doi.org/10.1016/0045-7930(94)00032-T.

[35] ITTC, “ITTC-Recommended procedures and guidelines practical guidelines for ship CFD applications,” 2011. Accessed: Apr. 26, 2023. [Online]. Available: https://ittc.info/media/1357/75-03-02-03.pdf

[36] L. F. Richardson and R. T. Glazebrook, “On the approximate arithmetical solution by finite differences of physical problems involving differential equations, with an application to the stresses in a masonry dam,” *Proceedings of the Royal Society of London. Series A, Containing Papers of a Mathematical and Physical Character*, vol. 83, no. 563, pp. 335–336, Jan. 1997, doi: 10.1098/rspa.1910.0020.

[37] P. J. Roache, “Verification of codes and calculations,” *AIAA Journal*, vol. 36, no. 5, pp. 696–702, 1998, doi: 10.2514/2.457.

[38] I. Celik, U. Ghia, P. J. Roache, C. Freitas, H. Coloman, and P. Raad, “Procedure of estimation and reporting of uncertainty due to discretization in CFD applications,” *J. Fluids Eng.*, vol. 130, p. 078001, Jul. 2008, doi: 10.1115/1.2960953.

[39] A. DOGRUL, “Hydrodynamic investigation of a submarine moving under free surface,” *Journal of Eta Maritime Science*, vol. 7, no. 3, pp. 212–226, 2019, doi: 10.5505/jems.2019.42204.

[40] H. L. Liu and T. T. Huang, “Summary of DARPA Suboff experimental program data,” Naval Surface Warfare Center Carderock Division (NSWCCD), West Bethesda, MD, USA, Jun. 1998.

PUBLICATIONS FROM THE THESIS

Conference Papers

1. K. E. Ozlu, A. G. Avcı, S. Mancini, (2024) Numerical Investigation of the Effect of Flow-Induced Noise in the Form of a Submarine On Free Surface and Depth. 14. Uluslararası Akademik Araştırmalar Kongresi (ICAR), Ankara